



HAL
open science

Study of the Effect of Thermal Dispersion on Internal Natural Convection in Porous Media Using Fourier Series

Marwan Fahs, Thomas Graf, Tuong Vi Tran, Behzad Ataie-Ashtiani, Craig.T. Simmons, Anis Younes

► **To cite this version:**

Marwan Fahs, Thomas Graf, Tuong Vi Tran, Behzad Ataie-Ashtiani, Craig.T. Simmons, et al.. Study of the Effect of Thermal Dispersion on Internal Natural Convection in Porous Media Using Fourier Series. *Transport in Porous Media*, 2020, 131, pp.537-568. 10.1007/s11242-019-01356-1 . hal-03044964

HAL Id: hal-03044964

<https://hal.science/hal-03044964>

Submitted on 9 Dec 2020

HAL is a multi-disciplinary open access archive for the deposit and dissemination of scientific research documents, whether they are published or not. The documents may come from teaching and research institutions in France or abroad, or from public or private research centers.

L'archive ouverte pluridisciplinaire **HAL**, est destinée au dépôt et à la diffusion de documents scientifiques de niveau recherche, publiés ou non, émanant des établissements d'enseignement et de recherche français ou étrangers, des laboratoires publics ou privés.



Study of the Effect of Thermal Dispersion on Internal Natural Convection in Porous Media Using Fourier Series

Marwan Fahs¹ · Thomas Graf² · Tuong Vi Tran² · Behzad Ataie-Ashtiani^{3,4} · Craig. T. Simmons⁴ · Anis Younes^{1,5,6}

Received: 28 March 2019 / Accepted: 22 October 2019
© Springer Nature B.V. 2019

Abstract

Natural convection in a porous enclosure in the presence of thermal dispersion is investigated. The Fourier–Galerkin (FG) spectral element method is adapted to solve the coupled equations of Darcy’s flow and heat transfer with a full velocity-dependent dispersion tensor, employing the stream function formulation. A sound implementation of the FG method is developed to obtain accurate solutions within affordable computational costs. In the spectral space, the stream function is expressed analytically in terms of temperature, and the spectral system is solved using temperature as the primary unknown. The FG method is compared to finite element solutions obtained using an in-house code (TRACES), OpenGeoSys and COMSOL Multiphysics[®]. These comparisons show the high accuracy of the FG solution which avoids numerical artifacts related to time and spatial discretization. Several examples having different dispersion coefficients and Rayleigh numbers are tested to analyze the solution behavior and to gain physical insight into the thermal dispersion processes. The effect of thermal dispersion coefficients on heat transfer and convective flow in a porous square cavity has not been investigated previously. Here, taking advantage of the developed FG solution, a detailed parameter sensitivity analysis is carried out to address this gap. In the presence of thermal dispersion, the Rayleigh number mainly affects the convective velocity and the heat flux to the domain. At high Rayleigh numbers, the temperature distribution is mainly controlled by the longitudinal dispersion coefficient. Longitudinal dispersion flux is important along the adiabatic walls while transverse dispersion dominates the heat flux toward the isothermal walls. Correlations between the average Nusselt number and dispersion coefficients are derived for three Rayleigh number regimes.

Keywords Natural convection · Thermal dispersion · Darcy’s law · Fourier series solution · COMSOL multiphysics · Parameter sensitivity analysis · Nusselt number

List of Symbols

A_{disp}^{XX} Coefficient of the non-dimensional dispersion tensor
 A_{disp}^{XZ} Coefficient of the non-dimensional dispersion tensor

Extended author information available on the last page of the article

28	A_{disp}^{ZZ}	Coefficient of the non-dimensional dispersion tensor
29	A_L	Non-dimensional longitudinal dispersion coefficient
30	$B_{m,n}$	Fourier series coefficient—stream function
31	$\tilde{B}_{g,h}$	Matrix coefficient defined in “Appendix A”
32	$C_{r,s}$	Fourier series coefficient—temperature
33	Er_{Nu}	Relative error on Nusselt number
34	$Er_{\theta^{\text{top}}}$	Relative error on temperature at the top wall
35	$Er_{U^{\text{top}}}$	Relative error on horizontal velocity at the top wall
36	$Er_{V^{\text{top}}}$	Relative error on vertical velocity at the top wall
37	F^{Disp}	Function including all dispersion terms
38	g	Gravitational acceleration
39	H	Square size
40	h	Local convection coefficient
41	\mathbf{I}	Identity tensor
42	K	Permeability
43	N_m	Number of Fourier modes in z —stream function
44	N_n	Number of Fourier modes in x —stream function
45	N_p	Number of integration points
46	N_r	Number of Fourier modes in z —temperature
47	N_s	Number of Fourier modes in x —temperature
48	Nu	Local Nusselt number
49	$\overline{\text{Nu}}$	Average Nusselt number
50	n_A	Polynomial degree for A_L
51	n_R	Polynomial degree for $R_{\alpha_{\text{disp}}}$
52	p	Fluid pressure
53	$P_{i,j}$	Polynomial coefficient of the scaling relation
54	Ra	Rayleigh number
55	R^F	Residual of the flow equation
56	R^H	Residual of the heat equation
57	$R_{g,h}^F$	Residual of the spectral flow equation
58	$R_{g,h}^H$	Residual of the spectral heat equation
59	$R_{\alpha_{\text{disp}}}$	Ratio of the transverse to longitudinal dispersion
60	T	Temperature
61	T_h	Hot temperature at the left wall
62	T_c	Cold temperature at the right wall
63	u	Horizontal velocity component
64	U	Non-dimensional horizontal velocity
65	U^{top}	Non-dimensional horizontal velocity—top wall
66	U^{max}	Maximum horizontal velocity
67	v	Vertical velocity
68	V	Non-dimensional vertical velocity
69	V^{hot}	Non-dimensional vertical velocity—hot wall
70	V^{max}	Maximum non-dimensional vertical velocity
71	\vec{V}	Darcy’s velocity
72	$ \vec{V} $	Magnitude of velocity vector
73	Wp_i	Weight integration function
74	x, X	Abscissa, non-dimensional abscissa
75	z, Z	Elevation, non-dimensional elevation

76	Xp_i, Zp_i	Coordinates of integration points
77	α_L, α_T	Longitudinal and transverse dispersion
78	α_m	Effective thermal diffusivity
79	α_{disp}	Dispersion tensor
80	β	Thermal expansion
81	$\beta_{g,m,r}^I$	Matrix coefficient defined in “Appendix A”
82	$\beta_{g,m,r}^{II}$	Matrix coefficient defined in “Appendix A”
83	$\delta_{i,j}$	Kronecker delta function
84	ε^g	Vector coefficient defined in “Appendix A”
85	θ	Non-dimensional temperature
86	θ^{top}	Non-dimensional temperature at the top wall
87	Θ	Shifted non-dimensional temperature
88	λ_{surf}	Thermal conductivity
89	$\Lambda_{h,s}$	Matrix coefficient defined in “Appendix A”
90	μ	Fluid viscosity
91	ρ	Fluid density
92	ρ_c	Fluid density at the cold temperature
93	σ	Ratio of heat capacity porous material to fluid
94	φ	Stream function
95	Φ	Non-dimensional stream function
96	$\chi_{h,n,s}^I$	Matrix coefficient defined in “Appendix A”
97	$\chi_{h,n,s}^{II}$	Matrix coefficient defined in “Appendix A”

1 Introduction

Natural convection (NC) in saturated porous media is gaining increased attention because of its wide range of applications in petroleum production, geothermal energy, geologic carbon sequestration, nuclear waste disposal, thermal insulation systems, nuclear reactors, oxide fuel cells, solar collectors and biomedical technologies, among many others. Comprehensive reviews on NC in porous media and its applications can be found in Nield and Simmons (2018), Ataie-Ashtiani et al. (2018), Nield and Bejan (2017), Vafai (2011, 2015), Vadász (2008) and Ingham and Pop (2005). In the last two decades, numerical modeling has emerged as a key tool to tackle the aforementioned applications. Nowadays, numerical modeling is commonly used to understand NC processes and in several engineering applications such as designing, planning, site investigation, safety report assessment and predictive simulations. The analysis of many applications of NC in porous media is often based on the constant thermal diffusivity model which neglects thermal dispersion effects. This simplification reduces the computational complexity introduced by the nonlinearity of the thermal dispersion terms. However, the obvious disadvantage is that the constant thermal diffusivity assumption is not appropriate to describe mixing processes (Thiele 1997; Sheremet et al. 2017; Wen et al. 2018).

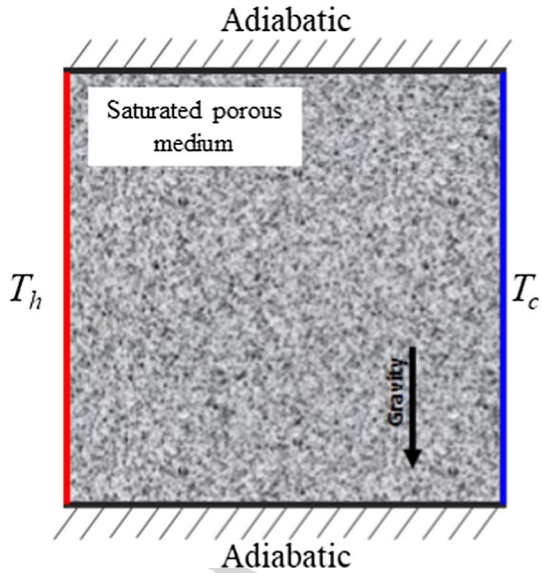
Thermal dispersion effects are caused by mechanical mixing of the interstitial fluid at the pore scale. This mixing is mainly related to obstructions introduced by tortuosity of the porous medium. It can also be caused by recirculation generated by low pressure in local regions arising from flow restrictions. A detailed review on thermal dispersion in porous media can be found in Nield and Bejan (2017). Thermal dispersion processes are usually modeled as a full velocity-dependent tensorial quantity, with two components either paral-

121 lel (longitudinal) or orthogonal (transverse) to the flow direction. Several experimental and
 122 modeling studies have been conducted to derive the thermal dispersion tensor and/or to esti-
 123 mate the transverse and longitudinal dispersion coefficients depending on the porous media
 124 skeleton (e.g., Ozgumus and Mobedi 2016; DeGroot and Straatman 2012). Cheng (1981),
 125 Hsiao (1998) and Languri and Pillai (2014) have compared numerical simulations to labora-
 126 tory experiments and have shown that the derived thermal dispersion model provides the best
 127 agreement with experimental data. Many studies have highlighted the significant effect of
 128 thermal dispersion on natural (e.g., Sheremet et al. 2017; Khaled and Chamkha 2001; Abbas
 129 et al. 2009; Jha and Aina 2017), forced (e.g., Kuznetsov 2000; Cheng and Lin 2002; Hooman
 130 et al. 2017) or mixed convection in non-Darcian porous media (i.e., under a non-Darcian flow
 131 regime). Further studies have also shown that strong heat dispersion effects can occur at low
 132 pore velocity in the Darcian regime (Thiele 1997; Telles and Trevisan 1993; Sheremet et al.
 133 2016; Wang et al. 2016; Fajraoui et al. 2017). Given its significant effects on heat transfer
 134 processes and the advancement in computational techniques, the acknowledgement of ther-
 135 mal dispersion effects in the applications related to NC has been recently increased (e.g.,
 136 Sheremet et al. 2016, 2017; Molina-Giraldo et al. 2011; Özerinç et al. 2012). The simulation
 137 of thermal dispersion has become available in several software packages such as COMSOL
 138 Multiphysics, FLUENT, FEFLOW (Diersch 2014) and OpenGeoSys (Sachse et al. 2015;
 139 Kolditz et al. 2012), among others.

140 Thermal dispersion effects have been investigated for problems involving external NC
 141 (e.g., Cheng 1981; Plumb 1983; Mohammadien and EL-Amin 2000; El-Hakim 2001; Asbik
 142 et al. 2007). Thermal dispersion associated to internal NC remains poorly understood, par-
 143 ticularly relative to studies of external NC or forced convection. Furthermore, despite the
 144 increasing interest in the simulation of thermal dispersion processes, there is no reference
 145 benchmark solution that can be used to verify the simulation results. The popular problem
 146 of NC in square porous cavity is a typical example of internal NC (Baïri et al. 2014). This
 147 problem describes convective flow in a square porous domain subject to differentially heated
 148 vertical walls. Due to its simplified boundary conditions and geometry and due to the large
 149 number of published numerical solutions based on a variety of numerical methods (Fahs et al.
 150 2014; Wang et al. 2018), this problem has been accepted to be a common benchmark for
 151 NC codes in the case of constant thermal diffusivity (Zhu et al. 2017). It is also widely used
 152 to provide consistent physical understanding of the NC processes in a porous enclosure. To
 153 the best of our knowledge, the effect of thermal dispersion on this problem has never been
 154 studied. Thus, the main objectives of this work are (1) to develop a high-accuracy solution for
 155 the problem of NC in a square porous cavity in the presence of velocity-dependent thermal
 156 dispersion, and (2) to use this solution to understand the effect of thermal dispersion on NC
 157 processes in a porous enclosure.

158 The high-accuracy reference solution is derived using the Fourier–Galerkin (FG) spec-
 159 tral element method (Peyret 2013). The Galerkin integrals resulting for the dispersion terms
 160 are evaluated numerically using a high-order adaptive technique. An efficient approach is
 161 developed to solve the spectral system of equations and to deal with the nonlinearity of the
 162 convective and thermal dispersion terms. This approach is based on reducing the number
 163 of degrees of freedom and on an efficient algorithm for the evaluation of the Fourier series
 164 on the integration points. Several test cases, dealing with a variety of parameters, are gen-
 165 erated to understand the solution behavior and to provide a set of reference data for code
 166 verification. To build more confidence in the FG solution and to highlight its worthiness
 167 for code benchmarking, the generated test cases are simulated using an in-house advanced
 168 code (TRACES: Transport of RadioActive Elements in Subsurface), the finite element code
 169 OpenGeoSys (OGS) and COMSOL Multiphysics®. The developed FG solution is used to

Fig. 1 Conceptual model of the studied problem including heat boundary conditions. All boundaries are impermeable to fluid flow



170 carry out a detailed parameter sensitivity analysis in order to investigate the role of thermal
 171 dispersion coefficients on NC processes in a porous enclosure.

172 **2 Problem Description and Mathematical Model**

173 The problem geometry and boundary conditions are shown in Fig. 1. The square porous
 174 cavity of dimensional thickness H has adiabatic horizontal boundaries. It is assumed that
 175 the left and right boundaries are maintained at different temperatures T_h and T_c ($T_h > T_c$),
 176 respectively. Vertical and horizontal boundaries are impermeable. Darcy's law is assumed to
 177 hold. Flow is considered to be saturated and within the Boussinesq approximation limits.
 178 The porous skeleton is incompressible. Local thermal equilibrium in the porous medium is
 179 assumed. Under these assumptions, the governing equations are given by (Mahmud and Pop
 180 2006; Rossa et al. 2017):

182
$$\vec{\nabla} \cdot \vec{\nabla} = 0 \tag{1}$$

183
$$\vec{\nabla} = -\frac{K}{\mu} \vec{\nabla} (p + \rho g z) \tag{2}$$

185
$$\sigma \frac{\partial T}{\partial t} + \vec{\nabla} \cdot \vec{\nabla} T - \vec{\nabla} \cdot (\alpha_m \mathbf{I} + \alpha_{\text{disp}}) \vec{\nabla} T = 0 \tag{3}$$

188
$$\rho = \rho_c [1 - \beta(T - T_c)] \tag{4}$$

189 where $\vec{\nabla}$ is velocity vector, p is fluid pressure, T is temperature, K is permeability, μ is fluid
 190 viscosity, g is gravitational acceleration, ρ is fluid density, σ is the ratio of the composite
 191 material heat capacity to the convective fluid heat capacity, α_m is effective thermal diffusivity,
 192 \mathbf{I} is the identity tensor, α_{disp} is dispersion tensor, ρ_c is fluid density at the cold temperature
 193 T_c and β is thermal expansion coefficient.

194 Thermal dispersion processes can be described using the Scheidegger model (Scheidegger
 195 1961) that assumes isotropic dispersion processes. In the present work, thermal dispersion is

acknowledged via the Bear–Scheidegger model (Bear and Bachmat 1990; Emami-Meybodi 2017). This model suggests that dispersion results in greater mixing in the direction of flow than in the transverse direction. The anisotropic dispersion tensor is defined as:

$$\alpha_{\text{disp}} = (\alpha_L - \alpha_T) \frac{\vec{\mathbf{V}} \times \vec{\mathbf{V}}}{|\vec{\mathbf{V}}|} + \alpha_T |\vec{\mathbf{V}}| \mathbf{I} \quad (5)$$

where α_L and α_T are the longitudinal and transverse dispersion coefficients, respectively.

3 The Fourier–Galerkin (FG) Solution

The developed solution is based on the spectral element FG method. Spectral methods combine the exactness of the analytical methods with an important extent of generality in describing the geometry and boundary conditions as with numerical methods (BniLam and Al-Khoury 2017). Spectral methods present a significant interest in accurately solving the equations of flow, mass and heat transfer in porous media (Fahs et al. 2014; Wang et al. 2018; BniLam, and Al-Khoury 2017; Shao et al. 2015, 2016; Ameli et al. 2013, 2018). Detailed description of the use of spectral methods for solving partial differential equations as well as the implementation of these methods can be found in Kopriva (2009) and Peyret (2013). The solution procedure is described in four steps as outlined below.

3.1 Stream Function Formulation and Non-dimensional Equations

The continuity equation can be intrinsically satisfied using the stream function (φ), which is defined as:

$$u = \frac{\partial \varphi}{\partial z}; v = -\frac{\partial \varphi}{\partial x} \quad (6)$$

where u and v are the components of the velocity vector ($\vec{\mathbf{V}}$).

The non-dimensional equations can be derived by assuming that buoyancy is the primary force. This can be achieved using the following dimensionless variables:

$$X = \frac{x}{H}; Z = \frac{z}{H}; \Phi = \frac{\varphi}{\alpha_m}; \theta = \frac{T - T_c}{T_h - T_c}; U = \frac{u \cdot H}{\alpha_m}; V = \frac{v \cdot H}{\alpha_m} \quad (7)$$

Thus, the stream function formulation of the non-dimensional flow and heat transfer equations (at steady-state conditions) can be written as:

$$\frac{\partial^2 \Phi}{\partial X^2} + \frac{\partial^2 \Phi}{\partial Z^2} = -\text{Ra} \frac{\partial \theta}{\partial X} \quad (8)$$

$$\begin{aligned} \frac{\partial \Phi}{\partial Z} \frac{\partial \theta}{\partial X} - \frac{\partial \Phi}{\partial X} \frac{\partial \theta}{\partial Z} - \left(\frac{\partial^2 \theta}{\partial X^2} + \frac{\partial^2 \theta}{\partial Z^2} \right) - \frac{\partial}{\partial X} \left(A_{\text{disp}}^{XX} \frac{\partial \theta}{\partial X} + A_{\text{disp}}^{XZ} \frac{\partial \theta}{\partial Z} \right) \\ - \frac{\partial}{\partial Z} \left(A_{\text{disp}}^{XZ} \frac{\partial \theta}{\partial X} + A_{\text{disp}}^{ZZ} \frac{\partial \theta}{\partial Z} \right) = 0 \end{aligned} \quad (9)$$

where $\text{Ra} = \frac{KHg\rho_c\beta(T_h - T_c)}{\mu\alpha_m}$ is the porous medium Rayleigh number representing the ratio of the buoyancy to diffusion.

231 A_{disp}^{XX} , A_{disp}^{XZ} and A_{disp}^{ZZ} are the coefficients of the non-dimensional dispersion tensor, given
 232 as:

233
$$A_{disp}^{XX} = \frac{\alpha_{disp}^{xx}}{\alpha_m} = A_L \left(\frac{U^2}{\sqrt{U^2 + V^2}} + R_{\alpha_{disp}} \frac{V^2}{\sqrt{U^2 + V^2}} \right) \quad (10)$$

236
$$A_{disp}^{ZZ} = \frac{\alpha_{disp}^{zz}}{\alpha_m} = A_L \left(\frac{V^2}{\sqrt{U^2 + V^2}} + R_{\alpha_{disp}} \frac{U^2}{\sqrt{U^2 + V^2}} \right) \quad (11)$$

238
$$A_{disp}^{XZ} = \frac{\alpha_{disp}^{xz}}{\alpha_m} = A_L (1 - R_{\alpha_{disp}}) \frac{UV}{\sqrt{U^2 + V^2}} \quad (12)$$

239 where $A_L = \alpha_L / H$ and $R_{\alpha_{disp}} = \alpha_T / \alpha_L$ are non-dimensional longitudinal coefficient and
 240 ratio of the transverse dispersion coefficient to the longitudinal dispersion coefficient.

241 A_{disp}^{XX} , A_{disp}^{XZ} and A_{disp}^{ZZ} can be expressed in terms of the stream function using:

243
$$U = \frac{\partial \Phi}{\partial Z}; \quad V = -\frac{\partial \Phi}{\partial X} \quad (13)$$

244 Equations (8) and (9) are subject to the following boundary conditions:

245
$$X = 0 \rightarrow \Phi = 0; \theta = 1$$

 246
$$X = 1 \rightarrow \Phi = 0; \theta = 0$$

 248
$$Z = 0, 1 \rightarrow \Phi = 0; \partial \theta / \partial Z = 0 \quad (14)$$

249 **3.2 Change of Variable: Homogeneous Boundary Conditions**

250 Homogeneous boundary conditions are required for the FG method (Peyret 2013). This is
 251 satisfied for the stream function. For the heat transport equation, as in Fahs et al. (2014), we
 252 applied the following temperature change of variable:

254
$$\Theta = \theta + X - 1 \quad (15)$$

255 Introducing the residuals for flow (R^F) and heat transfer (R^H) equations and using the
 256 new variable Θ , Eqs. (8) and (9) become:

258
$$R^F = \frac{\partial^2 \Phi}{\partial X^2} + \frac{\partial^2 \Phi}{\partial Z^2} + Ra \frac{\partial \Theta}{\partial X} - Ra = 0 \quad (16)$$

259
$$R^H = \frac{\partial^2 \Theta}{\partial X} + \frac{\partial^2 \Theta}{\partial Z} - \frac{\partial \Phi}{\partial Z} \frac{\partial \Theta}{\partial X} + \frac{\partial \Phi}{\partial X} \frac{\partial \Theta}{\partial Z} + \frac{\partial \Phi}{\partial Z}$$

 260
$$+ A_{disp}^{XX} \frac{\partial^2 \Theta}{\partial X^2} + 2A_{disp}^{XZ} \frac{\partial^2 \Theta}{\partial X \partial Z} + A_{disp}^{ZZ} \frac{\partial^2 \Theta}{\partial Z^2}$$

 261
$$+ \left(\frac{\partial A_{disp}^{XX}}{\partial X} + \frac{\partial A_{disp}^{XZ}}{\partial Z} \right) \frac{\partial \Theta}{\partial X} + \left(\frac{\partial A_{disp}^{XZ}}{\partial X} + \frac{\partial A_{disp}^{ZZ}}{\partial Z} \right) \frac{\partial \Theta}{\partial Z}$$

 263
$$- \frac{\partial A_{disp}^{XX}}{\partial X} - \frac{\partial A_{disp}^{XZ}}{\partial Z} = 0 \quad (17)$$

264 The derivatives of the dispersion tensor coefficients with respect to X and Z are calculated
 265 as:

268
$$\frac{\partial A_{disp}^{XX}}{\partial X} = \frac{2}{\sqrt{U^2 + V^2}} A_L \left(U \frac{\partial U}{\partial X} + R_{\alpha_{disp}} V \frac{\partial V}{\partial X} \right) - \frac{A_{disp}^{XX}}{(U^2 + V^2)} \left(U \frac{\partial U}{\partial X} + V \frac{\partial V}{\partial X} \right) \quad (18)$$

Author Proof

$$\frac{\partial A_{\text{disp}}^{ZZ}}{\partial Z} = \frac{2}{\sqrt{U^2 + V^2}} A_L \left(R_{\alpha_{\text{disp}}} U \frac{\partial U}{\partial Z} + V \frac{\partial V}{\partial Z} \right) - \frac{A_{\text{disp}}^{ZZ}}{U^2 + V^2} \left(U \frac{\partial U}{\partial Z} + V \frac{\partial V}{\partial Z} \right) \quad (19)$$

$$\frac{\partial A_{\text{disp}}^{XZ}}{\partial X} = A_L \frac{1 - R_{\alpha_{\text{disp}}}}{\sqrt{U^2 + V^2}} \left(V \frac{\partial U}{\partial X} + U \frac{\partial V}{\partial X} \right) - \frac{A_{\text{disp}}^{XZ}}{U^2 + V^2} \left(U \frac{\partial U}{\partial X} + V \frac{\partial V}{\partial X} \right) \quad (20)$$

$$\frac{\partial A_{\text{disp}}^{XZ}}{\partial Z} = A_L \frac{1 - R_{\alpha_{\text{disp}}}}{\sqrt{U^2 + V^2}} \left(V \frac{\partial U}{\partial Z} + U \frac{\partial V}{\partial Z} \right) - \frac{A_{\text{disp}}^{XZ}}{U^2 + V^2} \left(U \frac{\partial U}{\partial Z} + V \frac{\partial V}{\partial Z} \right) \quad (21)$$

With the new variable Θ , the thermal boundary conditions become:

$$\begin{aligned} X = 0, 1 &\rightarrow \Theta = 0 \\ Z = 0, 1 &\rightarrow \partial\Theta / \partial Z = 0 \end{aligned} \quad (22)$$

3.3 The FG Method

The unknowns Φ and Θ now have homogeneous boundary conditions. The problem is also spatially periodic. Thus, Φ and Θ can be approximated by truncated double Fourier series that satisfy the boundary conditions, written as follows:

$$\Phi(X, Z) = \sum_{m=1}^{N_m} \sum_{n=1}^{N_n} B_{m,n} \sin(m\pi Z) \sin(n\pi X) \quad (23)$$

$$\Theta(X, Z) = \sum_{r=0}^{N_r} \sum_{s=1}^{N_s} C_{r,s} \cos(r\pi Z) \sin(s\pi X) \quad (24)$$

where N_m (resp. N_r) and N_n (resp. N_s) are the number of Fourier series modes (FSMs) in the X and Z directions for the stream function (resp. temperature). $B_{m,n}$ and $C_{r,s}$ are the Fourier series coefficients for the stream function and temperature, respectively.

The coefficients $B_{m,n}$ and $C_{r,s}$ can be calculated using a Galerkin-type technique, based on the orthogonality property of the cosine and sine functions. The Fourier series are substituted into Eqs. (16) and (17). Then, the residuals (R^F and R^T) are projected into the vector space of the FSMs and set to be zero in the average sense:

$$\begin{aligned} R_{g,h}^F &= \langle R^F, 4 \sin(g\pi Z) \sin(h\pi X) \rangle \\ &= 4 \int_0^1 \int_0^1 R^F \sin(g\pi Z) \sin(h\pi X) dXdZ = 0 \quad g = 1 \dots N_m; h = 1 \dots N_n \end{aligned} \quad (25)$$

$$\begin{aligned} R_{g,h}^H &= \langle R^H, 4 \cos(g\pi Z) \sin(h\pi X) \rangle \\ &= 4 \int_0^1 \int_0^1 R^H \cos(g\pi Z) \sin(h\pi X) dXdZ = 0, \quad g = 1 \dots N_r; h = 1 \dots N_s \end{aligned} \quad (26)$$

The Galerkin integrals arising from Eq. (25) as well as the ones related to the diffusion and convection terms in Eq. (26) [the first five terms in Eq. (17)] can be evaluated analytically. However, because of the nonlinear dependence of the dispersion tensor to velocity components, the integrals related to thermal dispersion cannot be evaluated in a closed form. Thus,

we resorted to numerical integration. This yields the following nonlinear spectral system [for more details readers can refer to Peyret (2013), Fahs et al. (2014) and Shao et al. (2015)]:

$$\begin{aligned}
 R_{g,h}^F &= -\pi^2(h^2 + g^2)B_{g,h} + \frac{\text{Ra}}{\pi} \sum_{r=0}^{N_r} \sum_{s=1}^{N_s} s \Lambda_{h,s} \Lambda_{g,r} C_{r,s} \\
 &\quad - \frac{\text{Ra}}{\pi^2} A_{g,0} \Lambda_{h,0} = 0 \quad g = 1 \dots N_m, h = 1 \dots N_n \quad (27) \\
 R_{g,h}^H &= -\varepsilon^g \pi^2 C_{g,h} (g^2 + h^2) - \frac{\pi^2}{4} \sum_{m=1}^{N_m} \sum_{n=1}^{N_n} \sum_{r=0}^{N_r} \sum_{s=1}^{N_s} s \cdot m \cdot \beta_{g,m,r}^I \chi_{h,n,s}^I B_{m,n} C_{r,s} \\
 &\quad - \frac{\pi^2}{4} \sum_{m=1}^{N_m} \sum_{n=1}^{N_n} \sum_{r=0}^{N_r} \sum_{s=1}^{N_s} n \cdot r \cdot \beta_{g,m,r}^{II} \chi_{h,n,s}^{II} B_{m,n} C_{r,s} + \pi g \tilde{B}_{g,h} \\
 &\quad + 4 \sum_{i=1}^{N_p} W_{p_i} F^{\text{Disp}}(X_{p_i}, Z_{p_i}) \cos(g\pi Z_{p_i}) \sin(h\pi X_{p_i}) = 0, \quad g = 0 \dots N_r, h = 1 \dots N_s \quad (28)
 \end{aligned}$$

The coefficients of Eqs. (27) and (28) are summarized in “Appendix A”. The numerical integrals of the dispersion terms appear as a Riemann sum in the last term of Eq. (28). In this sum, N_p is the number of integration points, (X_{p_i}, Z_{p_i}) are the coordinates of an integration point (i) and W_{p_i} is the corresponding weight function related to quadrature rule used for numerical integration. F^{Disp} is the function including all dispersion terms, given by:

$$\begin{aligned}
 F^{\text{Disp}}(X, Z) &= A_{\text{disp}}^{XX} \frac{\partial^2 \Theta}{\partial X^2} + 2A_{\text{disp}}^{XZ} \frac{\partial^2 \Theta}{\partial X \partial Z} + A_{\text{disp}}^{ZZ} \frac{\partial^2 \Theta}{\partial Z^2} \\
 &\quad + \left(\frac{\partial A_{\text{disp}}^{XX}}{\partial X} + \frac{\partial A_{\text{disp}}^{XZ}}{\partial Z} \right) \frac{\partial \Theta}{\partial X} + \left(\frac{\partial A_{\text{disp}}^{XZ}}{\partial X} + \frac{\partial A_{\text{disp}}^{ZZ}}{\partial Z} \right) \frac{\partial \Theta}{\partial Z} - \frac{\partial A_{\text{disp}}^{XX}}{\partial X} - \frac{\partial A_{\text{disp}}^{XZ}}{\partial Z} \quad (29)
 \end{aligned}$$

For ultimate accuracy and in order to avoid errors related to the numerical integration, we use an adaptive-order integration technique (Mousavi et al. 2012). With this technique, the number of integration points and the order of the Gauss–Kronrod rules are automatically updated to reach a prescribed accuracy.

3.4 Solving the Spectral System: Numerical Implementation

The FG method provides spectral accuracy for smooth solutions. However, a defect of this method is the Gibbs phenomena (Peyret 2013; Ameli et al. 2013) that can lead to instabilities (unphysical oscillations) for sharp solutions, as is the case for NC at high Rayleigh numbers. In such cases, stable solutions require a large number of FSMs for which the FG method is computationally impractical. Fahs et al. (2015) applied the FG method to solve the problem of NC in square porous cavity in the case of constant thermal diffusivity. They developed an efficient implementation of this method that allowed for using a large number of FSMs. Due to this implementation, they obtained solutions for high Rayleigh numbers (up to 10,000). Here we improve this implementation, and we extend it to deal with a velocity-dependent dispersion tensor. Thus, we reduce the number of degrees of freedom of the nonlinear spectral system by reformulating it with the Fourier coefficients of the shifted temperature ($C_{r,s}$) as the primary variables.

Author Proof

A closer look at Eq. (27) reveals that coefficients $B_{g,h}$ can be expressed analytically in terms of $C_{r,s}$. By substituting $B_{g,h}$ into Eq. (28), we can obtain a closed system of equations with $C_{r,s}$ as the primary variables. Thus, the nonlinear spectral system can be reduced to only the residual vector of the heat transfer equation. To solve this system, we use the efficient nonlinear solver of the IMSL library (<http://www.roguewave.com/products-services/imsl-numerical-libraries>). This solver is based on an advanced Newton's method which is the modified Powell hybrid algorithm. As in Fahs et al. (2015), we improve the performance and convergence of the solver by providing the analytical Jacobian matrix and by simplifying the four nested summations using the Kronecker delta properties.

A FORTRAN code is implemented to solve the spectral nonlinear system with the approaches and simplifications developed in the previous section. Some first runs of the code were carried out to verify its performance. These runs revealed that, despite the previous improvements, the code is still very impractical for cases involving velocity-dependent dispersion. For instance, one evaluation of the residual vector would take more than 10 h of CPU time, for $N_m = N_r = 50$ and $N_n = N_s = 100$ and for about 10,000 integration points.

Scrutiny of this matter revealed that the inefficiency of the code is related to the numerical integral procedure used to deal with the dispersion terms. As can be seen in Eq. (28), one residual evaluation requires $(N_r + 1) \times N_s$ evaluations of the dispersion term (F^{Disp}) on the integration points. The latter involves the Fourier series for both the stream function and the shifted temperature. This means that, if the standard integration procedure is applied, the Fourier series should be calculated on the integration points $(N_r + 1) \times N_s$ times. Thus, the corresponding number of operations is $N_p \times (N_r + 1) \times N_s \times [N_m \times N_n + (N_r + 1) \times N_s]$ times (i.e., 5×10^{11} in the previous example). In order to render the code practical, we implement a specific algorithm to reduce the number of evaluations of the Fourier series on the integration points (Fahs et al. 2016). The algorithm proceeds by evaluating F^{Disp} (via the Fourier series and their spatial first- and second-order derivatives) once when evaluating the first component of the heat transport residual vector ($R_{0,1}^H$). The values of F^{Disp} are then stored in a memory array and further used to calculate the other components of the residual vector. With this algorithm, the residual vector can be evaluated with $N_p \times [N_m \times N_n + (N_r + 1) \times N_s]$. For the previous example, this corresponds to 10^8 operations that require only 5 s of CPU time.

Finally, due to symmetrical boundary conditions, we can show analytically that the Fourier series coefficients ($B_{i,j}$ and $C_{i,j}$) for which the summation of indices ($i + j$) is even are equal to zero. We eliminate these coefficients and half the number of degrees of freedom.

3.5 Quantitative Indicators for Code Verification and Benchmarking

Prasad and Simmons (2005) highlighted the importance of quantitative indicators for code benchmarking compared to direct comparison of state variables maps due to the complexity of the instability processes and the qualitative nature of visual comparisons. Thus, we propose several objective metrics to assess heat transfer and flow processes which could be useful as quantitative indicators for code validation and benchmarking. The heat transfer processes are assessed using the average Nusselt number. The local Nusselt number (Nu) provides a measure of the convection heat flux occurring at the hot wall. It is defined as follows:

$$\text{Nu} = \frac{h}{\lambda_{\text{surf}}/H} \quad (30)$$

where h is the local convection coefficient and λ_{surf} is the thermal conductivity of the material forming the hot wall surface.

383 A common assumption is that λ_{surf} is equal to the equivalent thermal conductivity of the
 384 porous medium. The energy balance at the hot wall expresses the continuity of the conduction-
 385 dispersion flux at $X = 0^-$ and the convective flux (calculated via the Newton's cooling law)
 386 at $X = 0^+$. The non-dimensional form of the energy balance equation gives:

$$388 \quad Nu = \frac{h}{\lambda_{surf}/H} = \left(1 + A_{disp}^{XX}\right) \frac{\partial \theta}{\partial X} \Big|_{X=0} \quad (31)$$

389 Knowing that $U = 0$ at the hot wall (impervious boundary conditions), the local Nusselt
 390 number can be simplified to:

$$392 \quad Nu = \frac{h}{\lambda_{surf}/H} = \left(1 + A_L R_{\alpha_{disp}} |V|\right) \frac{\partial \theta}{\partial X} \Big|_{X=0} \quad (32)$$

393 This definition of local Nusselt number is similar to the one used in Howle and Georgiadis
 394 (1994) and Sheremet et al. (2016). By using the shifted temperature (Θ), Nu becomes:

$$396 \quad Nu = \frac{h}{\lambda_{surf}/H} = \left(1 + A_L R_{\alpha_{disp}} |V|\right) \left(\frac{\partial \Theta}{\partial X} - 1\right) \Big|_{X=0} \quad (33)$$

397 Nu can be evaluated using the Fourier series of Θ and Φ :

$$398 \quad Nu = \frac{h}{\lambda_{surf}/H}$$

$$399 \quad = \left(1 + A_L R_{\alpha_{disp}} \left| -\pi \sum_{m=1}^{N_m} \sum_{n=1}^{N_n} n B_{m,n} \sin(m\pi Z) \right| \right) \left(\pi \sum_{r=0}^{N_r} \sum_{s=1}^{N_s} s C_{r,s} \cos(r\pi Z) - 1 \right) \quad (34)$$

400 The average Nusselt number is given by:

$$402 \quad \overline{Nu} = \int_0^1 Nu \cdot dZ \quad (35)$$

403 The integral in Eq. (35) is evaluated numerically. The temperature distribution and con-
 404 vective fluid flow processes are assessed using the local values of temperature and velocity
 405 components at the centers of the top surface ($X = 0.5; Z = 1$) and hot wall ($X = 0; Z = 0.5$)
 406 and at the cavity center within the convective fluid flow. These metrics are calculated using
 407 the Fourier series as:

$$408 \quad \theta^{top} = \theta(X = 0.5; Z = 1) = \sum_{r=0}^{N_r} \sum_{s=1}^{N_s} (-1)^r \sin(s\pi/2) C_{r,s} + 0.5$$

$$409 \quad U^{top} = U(X = 0.5; Z = 1) = \pi \sum_{m=1}^{N_m} \sum_{n=1}^{N_n} m B_{m,n} (-1)^m \sin(n\pi/2);$$

$$410 \quad V^{hot} = V(X = 0; Z = 0.5) = -\pi \sum_{m=1}^{N_m} \sum_{n=1}^{N_n} n B_{m,n} \sin(m\pi/2) \quad (36)$$

412 4 Results and Discussion

413 Three matters are discussed in this section. We firstly investigate the stability of the FG
 414 solution in terms of the FSMs using six test cases. This step is important to confirm that

415 this solution is free of errors. The results of the six test cases are also useful to provide
 416 physical insight on the thermal dispersion processes. Secondly, we compare the FG solution
 417 against a discontinuous Galerkin finite element (DG) solution obtained using an advanced
 418 in-house research code (TRACES) and two standard finite element (FE) solutions based on
 419 OGS package and COMSOL Multiphysics[®] software. These comparisons are performed to
 420 give more confidence in the accuracy of our FG solution and to highlight its worthiness for
 421 code benchmarking and validation. Finally, we use the FG solution to develop a complete
 422 parameter sensitivity analysis and to understand the role of thermal dispersion coefficients
 423 on heat transfer and convective flow processes in a porous square cavity. In our analysis, we
 424 consider three levels of Rayleigh numbers (100, 1000 and 5000). As in Wang et al. (2018)
 425 and as it is common in the literature, these values are considered to investigate conduction-
 426 dominated, moderate and convection-dominated cases. We investigate different cases with
 427 A_L ranging from 0.01 to 1 and $R_{\alpha_{\text{disp}}}$ between 0.04 and 1. These ranges of variations are widely
 428 used in the literature (e.g., Abarca et al. 2007), and they are common for field conditions.

429 4.1 Test Cases: Solution Behavior and Understanding Thermal Dispersion Flux

430 Adequate FSMs should be used to obtain stable FG solutions and to avoid spurious oscillations
 431 related to the Gibbs phenomenon. Fahs et al. (2014, 2015) suggested an efficient technique
 432 to select the appropriate FSMs in the case of salinity-driven NC in porous square cavity and
 433 seawater intrusion in coastal aquifers, respectively. This technique proceeds by progressively
 434 increasing the number of FSMs until reaching a stable solution. The authors showed that the
 435 average Sherwood number (solute analogue of the average Nusselt number used in mass
 436 transfer) can be used as measure of solution stability. In this work, we adopt the same
 437 technique by replacing the Sherwood number by its equivalent in heat transfer, the Nusselt
 438 number.

439 We analyze the behavior of the FG solution via six test-case examples that cover the
 440 range of parameters variation. These cases deal with low, intermediate and high Rayleigh
 441 numbers (10^2 , 10^3 and 5×10^3 , respectively). For each Rayleigh number, we consider two
 442 cases involving, respectively, small ($A_L = \alpha_L / H = 0.001$) and high ($A_L = 1$) longitudinal
 443 dispersion coefficients. For all of these cases, and as is common in the literature, we consider
 444 $R_{\alpha_{\text{disp}}} = \alpha_T / \alpha_L = 0.1$ (Abarca et al. 2007).

445 For a low Rayleigh number ($Ra = 100$), stable solutions for both low and high dispersion
 446 cases are obtained using $N_m = N_r + 1 = 30$ and $N_n = N_s = 50$. As half of the Fourier
 447 coefficients are equal to zero (see previous section), the corresponding number of FSMs is
 448 1500. For $Ra = 1000$, in the case of small dispersion coefficient, the buoyancy forces become
 449 more important. This sharpens the temperature distribution and concentrates the streamlines
 450 in a thin layer toward the walls. The FG solution shows spurious oscillations introduced by the
 451 Gibbs phenomenon. The number of FSMs should be increased to remove these oscillations.
 452 In this case, the stable FG solution is obtained using 8000 FSMs ($N_m = N_r + 1 = 80$ and
 453 $N_n = N_s = 100$). For the high dispersion case, the solution is smoothed by the mixing
 454 processes induced by thermal dispersion. The Gibbs phenomenon completely disappears
 455 and a stable solution can be obtained with the same number of FSMs as in the low Rayleigh
 456 number case ($N_m = N_r + 1 = 30$ and $N_n = N_s = 50$). For $Ra = 5000$, 18,000 FSMs
 457 ($N_m = N_r + 1 = 120$ and $N_n = N_s = 150$) should be used to obtain a stable solution for
 458 the low dispersion case. For the high dispersion case, the FG solution is obtained using 3070
 459 FSMs ($N_m = N_r = 30$, $N_n = 60$ and $N_s = 140$).

460 For all cases, the numerical evaluation of the Galerkin integrals related to the dispersion
 461 terms is performed using a specific integration routine of the ISML library based on adaptive
 462 higher-order scheme. With this scheme, the domain is subdivided into a certain number of
 463 squares and on each square the number of integration points is locally updated to reach the
 464 prescribed accuracy. The number of integration points increases with the Rayleigh number.
 465 The solutions for the high dispersion cases involve more integration points than the low
 466 dispersion cases. For the low dispersion cases, about 6×10^3 points are used for $Ra = 100$, 10^4
 467 points are used for $Ra = 1000$ and 15×10^3 points are used for $Ra = 5000$. The corresponding
 468 solutions for the high dispersion cases involve about 10^4 , 2×10^4 and 32×10^3 points.

469 The streamlines and velocity field for the six test cases are plotted in Fig. 2. The cor-
 470 responding main isotherms (0.2, 0.4, 0.6 and 0.8) are depicted in Fig. 3. Figures 2 and 3
 471 show that for the low dispersion cases, the isotherms and streamlines look much like those
 472 obtained using the purely thermal diffusive model (Fahs et al. 2015). Closed streamlines and
 473 the velocity field show that, due to buoyancy effects, a clockwise-rotating cell is developed in
 474 the cavity. A slow-motion circulation zone can be observed at the core of the domain. For the
 475 low dispersion case, this zone expands diagonally from the bottom-left corner to the top-right
 476 one. The streamlines are highly dense at right-top and left bottom corners, indicating that in
 477 these zones the flow velocity reaches its maximum. The isotherms are not vertical but have
 478 almost a uniform shape. Due to the circulation of the fluid in place, the hot isotherms tilt
 479 upward to the right at the cavity top surface.

480 For the high dispersion case, the streamlines are less dense compared to the low
 481 dispersion case. This indicates that the thermal dispersion process dampens the fluid cir-
 482 culation, which is reasonable because dispersion enhances fluid mixing that dissipates
 483 buoyancy forces. This can be particularly observed at the top-left and bottom-right cor-
 484 ners where the streamlines are more distant from each other than in the low dispersion
 485 case. As a consequence of flow dampened, the zone of slow velocity in the core of the
 486 domain expands and becomes less directed toward the diagonal. Despite the fact that
 487 mixing processes related to thermal dispersion are dominating, in contrast to the purely
 488 diffusive model, the isotherms are not linear. They have an curved shape, which is com-
 489 pletely different from those observed with the pure diffusive model. In contrast to the
 490 case of low dispersion, the isotherms are not uniformly spaced. To understand the ori-
 491 gin of this behavior, we compare the isotherms of the velocity-dependent dispersion
 492 model with those obtained using a constant equivalent dispersion tensor. The coefficients
 493 of the constant dispersion tensor are calculated as averages of A_{disp}^{XX} , A_{disp}^{ZZ} and A_{disp}^{ZZ} over all
 494 the domain. For the high dispersion case ($Ra = 100$), the average values are calculated to
 495 be 7.8, 0.31 and 7.01, respectively. Figure 4 shows the comparison between the isotherms
 496 obtained using both models. It can be clearly seen that with the constant dispersion tensor
 497 the isotherms are uniformly spaced as in the pure diffusive model. Thus, this confirms that
 498 the zigzag shape of the isotherms is due to the velocity-dependent dispersion processes.

499 When the Rayleigh number is increased, for the low dispersion case, the streamlines
 500 get closer, indicating more intense fluid circulation. The increase in flow velocity shrinks
 501 the hydrodynamic boundary layer toward the hot and cold walls. The fluid circulation zone
 502 becomes confined toward the walls. The higher Rayleigh number can be seen as an increase
 503 in the buoyancy effects at constant diffusion coefficient. Since thermal dispersion is relatively
 504 weak, the isotherms become closely controlled by the flow structure. This explains their spiral
 505 shape (see Fig. 3). For the high dispersion case, the increase in Rayleigh number increases
 506 the flow velocity in the cavity. However, the isotherms are slightly sensitive to the Rayleigh
 507 number. This result is in agreement with Wen et al. (2018). In that paper, the authors, based
 508 on scaling analysis and direct numerical simulations, show that at sufficiently large Rayleigh

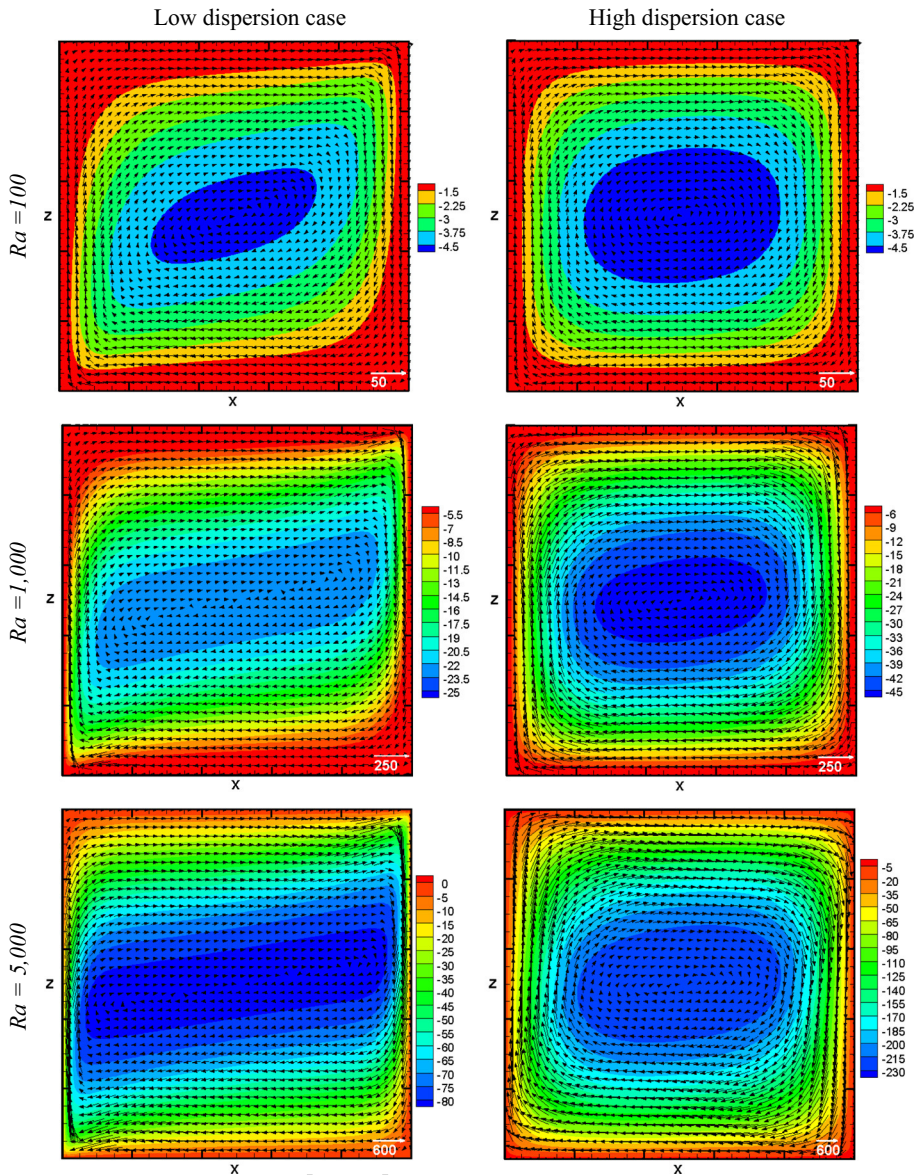


Fig. 2 The streamlines and velocity field for six test examples dealing with $Ra = 100$, 1000 and 5000 in the case of low dispersion ($A_L = 0.001$) and high dispersion ($A_L = 1$) coefficients ($R_{\alpha_{disp}} = 0.1$ for all cases)

509 number, the convection processes can be determined using the dispersive Rayleigh number.
 510 The latter is defined as the inverse of A_L .

511 The developed FG solution is used to gain an understanding of the dispersive heat flux in a
 512 convective cell. With the developed FG solution, the temperature and stream function can be
 513 expressed analytically in terms of the spatial directions. This allows for an accurate evaluation
 514 of the different components of the heat flux (namely the convective, diffusive and dispersive

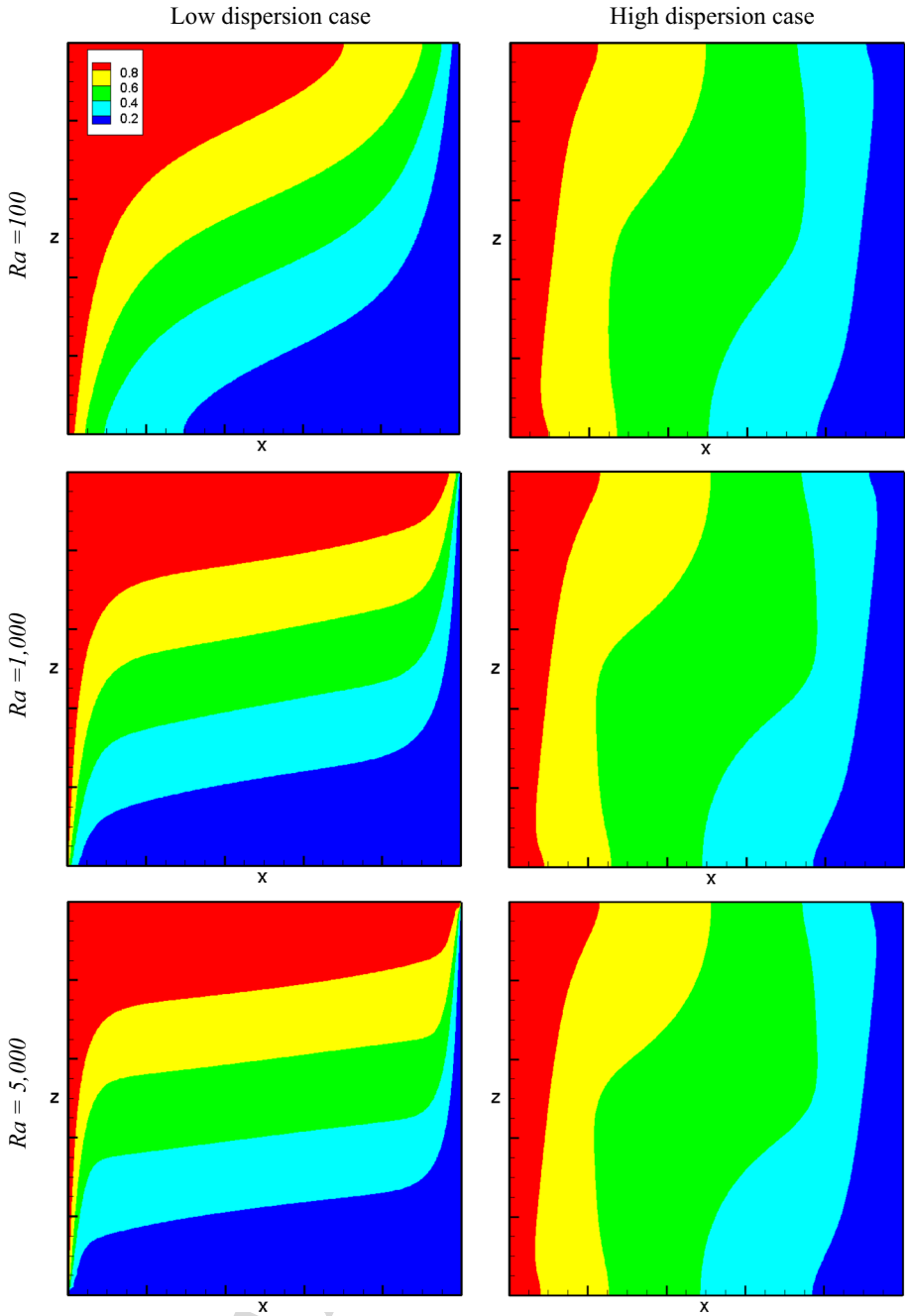
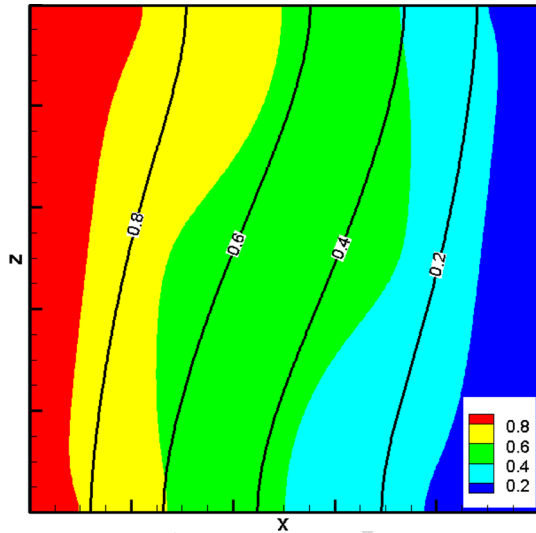


Fig. 3 The main isotherms (0.2, 0.4, 0.6 and 0.8) for six test examples dealing with $Ra = 100, 1000$ and 5000 in the case of low dispersion ($A_L = 0.001$) and high dispersion ($A_L = 1$) coefficients ($R_{\alpha_{disp}} = 0.1$ for all cases)

Fig. 4 Main isotherms (0.2, 0.4, 0.6 and 0.8) for $Ra = 100$, $A_L = 1$ and $R_{\alpha_{disp}} = 0.1$ (high dispersion case): comparison between the velocity-dependent dispersion model (color flood map) and the constant dispersion model (solid lines)



fluxes). The convective heat flux is well correlated to the velocity field. Thus, we focus on diffusive and dispersive fluxes. We only consider the high dispersion case which is more appropriate to observe the dispersion flux than the low dispersion case. Similar behaviors have been observed for the three values of Rayleigh number; thus, we consider $Ra = 100$.

Figure 5a shows the diffusive heat flux and its magnitude as well as the main isotherms. Figure 5b depicts the same patterns for the dispersive heat flux. Figure 5 shows that, for the case considered, the magnitude of the dispersive flux is one order of magnitude greater than that for the diffusive flux. The mixing between hot and cold fluid is dominated by thermal dispersion. Different behaviors can be observed for both fluxes. The diffusive flux is important around the highest and lowest isotherms in particular toward the bottom-left and top-right corners. Dispersive flux is important along the adiabatic walls. It exhibits its maximum amplitude toward the bottom-left and top-right corners (highest and lowest isotherms). The velocity is relatively weak at the center of the convective cell. Thus, the dispersive flux is almost zero in this zone. The dispersive heat flux coming from the hot wall is separated into two parts around the central zone (Fig. 5).

In Fig. 6, we distinguish between longitudinal and transverse dispersive fluxes. To understand the behavior of these fluxes, we include the velocity field and the thermal gradient in the same figure. This figure shows that the longitudinal flux that enhances mixing in the direction parallel to the velocity is important in the zones where the velocity is parallel to the thermal gradient (around the top and bottom surfaces, toward the top-right and bottom-left corners). The transverse dispersive flux, which acts in the direction orthogonal to the velocity, is important toward the vertical walls where the velocity is orthogonal to the thermal gradient. Figure 6a shows that longitudinal dispersion has no impact on heat transfer across the hot wall. This is mainly related to the diffusive flux and to transverse dispersion.

We should mention that, in contrast to standard numerical solution, the results in Figs. 5 and 6 have been obtained without any approximation due to the FG solution that provides the analytical expressions of the temperature and velocity field in terms of the spatial directions. This highlights the usefulness of the FG method and shows its flexibility for understanding physically the role of thermal dispersion on NC in a porous enclosure.

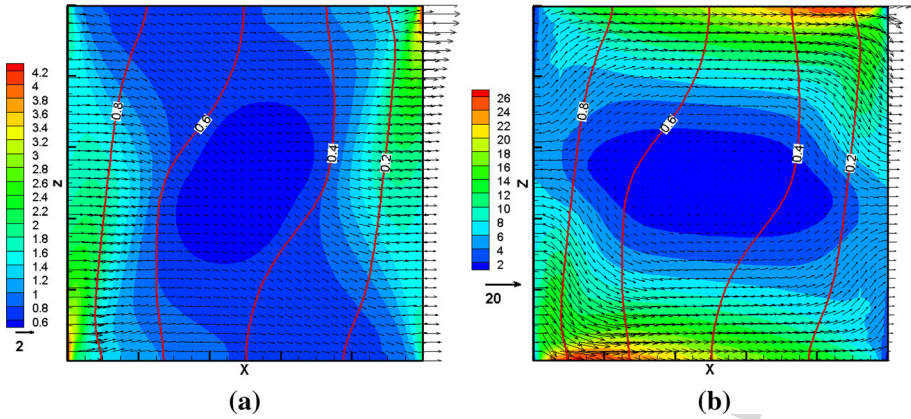


Fig. 5 Spatial distribution of the diffusive heat flux (a) and dispersive heat flux (b) for $Ra = 100$, $A_L = 1$ and $R_{\alpha_{disp}} = 0.1$ (high dispersion case): flux magnitude (color flood map), flux (arrows) and isotherms (contours)

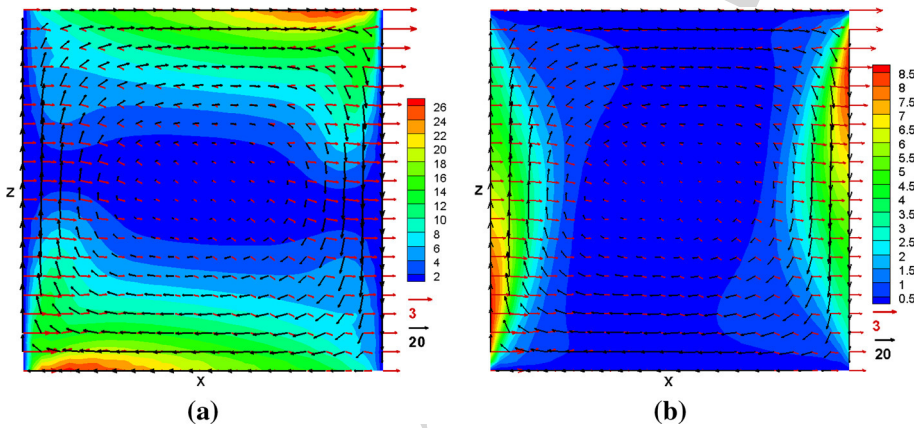


Fig. 6 Spatial distribution of the longitudinal dispersive flux (left) and transverse dispersive flux (right) for $Ra = 100$, $A_L = 1$ and $R_{\alpha_{disp}} = 0.1$ (high dispersion case): flux magnitude (color flood map), velocity (black arrows) and thermal gradient (red arrows)

544 **4.2 Benchmarking: Comparison with TRACES, OGS and COMSOL**

545 Benchmark reference solutions are valuable to give confidence in the accuracy of the numerical
 546 simulations, for the critical assessment of results derived from computer codes and for
 547 the improvement in the underlying numerical techniques (e.g., convergence studies). They
 548 are valuable to validate newly developed numerical techniques and to compare existing software.
 549 Benchmark reference solutions are also helpful for new software users to become
 550 familiarized with software interfaces and data processing. For heat transfer applications,
 551 reference solutions play a crucial role in testing the simulation procedure as most of the
 552 modeling studies are usually performed using a diverse suite of individual computer codes.
 553 Thus, benchmark reference solutions are essential to build confidence in the results of these
 554 codes and, consequently, on their physical insights and predictive outcomes gained from
 555 using them.

556 In this section, we evaluate the worthiness of the developed FG solutions in benchmarking
557 numerical codes. In fact, an effective benchmark should be unambiguous and representative
558 of physical processes. It is evident that the newly developed FG solution, including velocity-
559 dependent dispersion, is more representative of physical processes than existing reference
560 solutions based on the constant thermal diffusivity model. The development of local quanti-
561 tative metrics provides objective measures of the FG solution and makes it more suitable for
562 benchmarking. However, a common requirement for a useful benchmark is that it allows the
563 examination of the performance of the different numerical techniques implemented in differ-
564 ent codes. This section focuses on the evaluation of the ability of the proposed FG solution
565 for benchmarking numerical methods and techniques commonly used in codes. To do so,
566 we compare the FG solution against three numerical codes (TRACES, OGS and COMSOL
567 Multiphysics[®]) based on different numerical techniques. These codes are used. Transient
568 simulations are used in the three codes to avoid convergence issues related to steady-state
569 simulations encountered at high Rayleigh number and in high dispersion cases. Thus, the
570 transient system is allowed to evolve to reach steady-state conditions.

571 TRACES, developed by Hoteit et al. (2004), is a research code for flow and reactive
572 transport in saturated porous media. This code is based on advanced numerical methods
573 that reduce the numerical artifacts encountered with the standard Eulerian methods while
574 maintaining high performance. It is based on advanced numerical techniques for both spatial
575 discretization and time integration. In TRACES, the flow equations are discretized with the
576 mixed hybrid finite element method. This method is suitable to solve flow in porous media
577 and for coupling mass or heat transfer equation as it provides accurate and intrinsic evaluation
578 of the velocity field. For more details about the mixed hybrid finite element, please refer to
579 the review paper by Younes et al. (2010). The DG method (Miller et al. 2013) is used for the
580 discretization of the advection term. This method is suitable for the hyperbolic equation and
581 for solutions involving sharp fronts. It removes oscillations and reduces numerical diffusion
582 (Younes and Ackerer 2008; Nguyen et al. 2009; Dijoux et al. 2019). The diffusion–dispersion
583 term is discretized using the multipoint flux approximation method (MPFA). This method
584 is suitable for anisotropic problems and can be intrinsically coupled with the DG method
585 (Younes et al. 2009). For time integration, TRACES uses high-order methods via an advanced
586 ODE solver based on an adaptive time integration and time stepping scheme. The high-order
587 integration is coupled with the mixed hybrid and DG methods via the method of lines. More
588 details about this code can be found in Younes et al. (2009). TRACES has been used to
589 simulate NC in porous media in Fahs et al. (2015) and Shao et al. (2016, 2018). A structured
590 triangular mesh is used for TRACES simulations. This mesh is obtained by discretizing the
591 domain into several squares and by subdividing each square into four equal triangles.

592 OGS is a research and scientific framework for the development of numerical methods
593 for the simulation of thermo-hydro-mechanical-chemical processes in porous and fractured
594 media. OGS is a flexible FE framework for solving multi-field problems in porous and
595 fractured media for applications in geoscience and hydrology. In our OGS simulations, we
596 use a non-iterative adaptive time integration scheme based on error estimation (Hirthe and
597 Graf 2012). A uniform square mesh is used for the simulations with OGS.

598 COMSOL is a simulation software environment for multiphysics simulations. COMSOL
599 is increasingly used in applications related to NC or heat transfer in porous media (i.e., Tan
600 et al. 2012; Yacine et al. 2016). For the COMSOL simulations, we coupled the “Darcy’s
601 law” interface from the “subsurface flow” module to the “heat transfer in porous media”
602 interface from the “heat transfer” module. COMSOL is based on the FE method, but it offers
603 a variety of numerical techniques that can be used to solve the governing equations. In our
604 simulations, we used the default numerical scheme suggested in COMSOL (standard FE

method for spatial discretization, backward differentiation formula for time integration and fully coupled approach). An unstructured triangular mesh is used in COMSOL simulations.

The same test cases as in the previous section are simulated using TRACES, COMSOL and OGS. The physical parameters used in the three codes are summarized in “Appendix B”. Computational meshes involving an equivalent number of nodes are used in the three codes (about 10 K nodes).

Figure 7 illustrates the isotherms obtained using the FG method and the three codes (TRACES, COMSOL and OGS). The corresponding non-dimensional metrics (\overline{Nu} , θ^{top} , U^{top} and V^{top}) are summarized in Table 1. Also included in this table are the numerical errors for the three codes when considering the FG solution as the reference (error-free) solution. For $Ra = 100$ and in both low and high dispersion cases, Fig. 7 shows excellent agreement between all solutions regarding the isotherms. With errors less than 2%, Table 1 confirms the excellent agreement between the different solutions regarding the non-dimensional metrics. This result gives confidence in the accuracy of (1) the code developed for the FG solution, (2) the procedure used to select the FSMs, and (3) the technique used to include velocity-dependent dispersion (i.e., the numerical evaluation of Galerkin integrals related to the dispersion terms). The cases with $Ra = 100$ are simple from a computational point of view. The three codes achieve acceptable solutions even with relatively coarse meshes.

For higher Rayleigh ($Ra = 1000$ or 5000), with a relatively coarse mesh, OGS exhibits spurious/unphysical oscillations in the low dispersion cases. The same problem can be observed with COMSOL (Fig. 8). For equivalent computational meshes (same number of nodes), the oscillations with the square grid (in OGS) are larger than those with the triangular grid (in COMSOL). These oscillations are related to the standard FE method. They do not appear in TRACES as this is based on the DG method. To avoid oscillations in OGS, we used finer meshes (about 10 K). The instabilities disappear and physical temperatures (between 0 and 1) can be obtained but the solution remains inaccurate (Fig. 8b). A careful check of the numerical parameters reveals that this inconsistency is related to the time stepping procedure. This procedure allows for using large time step sizes for which the solution becomes inaccurate. To avoid this problem, OGS allows a maximum time step size. When this maximum step size is relatively small, OGS gives results which are in good agreement with the FG solution, as observed in Fig. 7. COMSOL allows for spurious oscillations to be removed by using a consistent stabilization technique that adds diffusion in the streamline direction. We used this technique with a mesh consisting of 10 K nodes, and we obtained a good agreement with the FG solution (Fig. 7). We should mention that the high dispersion cases are slightly sensitive to the computational mesh. However, for these cases, the computational efficiency of the solution becomes very dependent on the time integration scheme. In fact, for the high dispersion cases, the time required to reach the steady-state solution is much higher than the low dispersion cases. For longer transient simulations, we have observed that the higher-order integration schemes used in TRACES and COMSOL allow the use of large time step size and therefore reduce the computational cost. Table 1 also shows a good agreement between the non-dimensional metrics for $Ra = 1000$ (errors are less than 3%). For $Ra = 5000$ (low dispersion case), relatively weaker agreement can be observed between the different solutions, especially for the Nusselt number (errors are up to 13%). This could be attributed to the excessive numerical dispersion as for high Rayleigh numbers the convective term becomes dominant. The Nusselt numbers obtained with the three numerical codes are less than those obtained using the FG solution. This confirms that the discrepancy between the codes and FG solution is related to numerical dispersion. This numerical dispersion smooths out the temperature distribution and decreases the temperature gradient toward the hot wall. The discrepancy between TRACES and FG is less than those for COMSOL and OGS. This

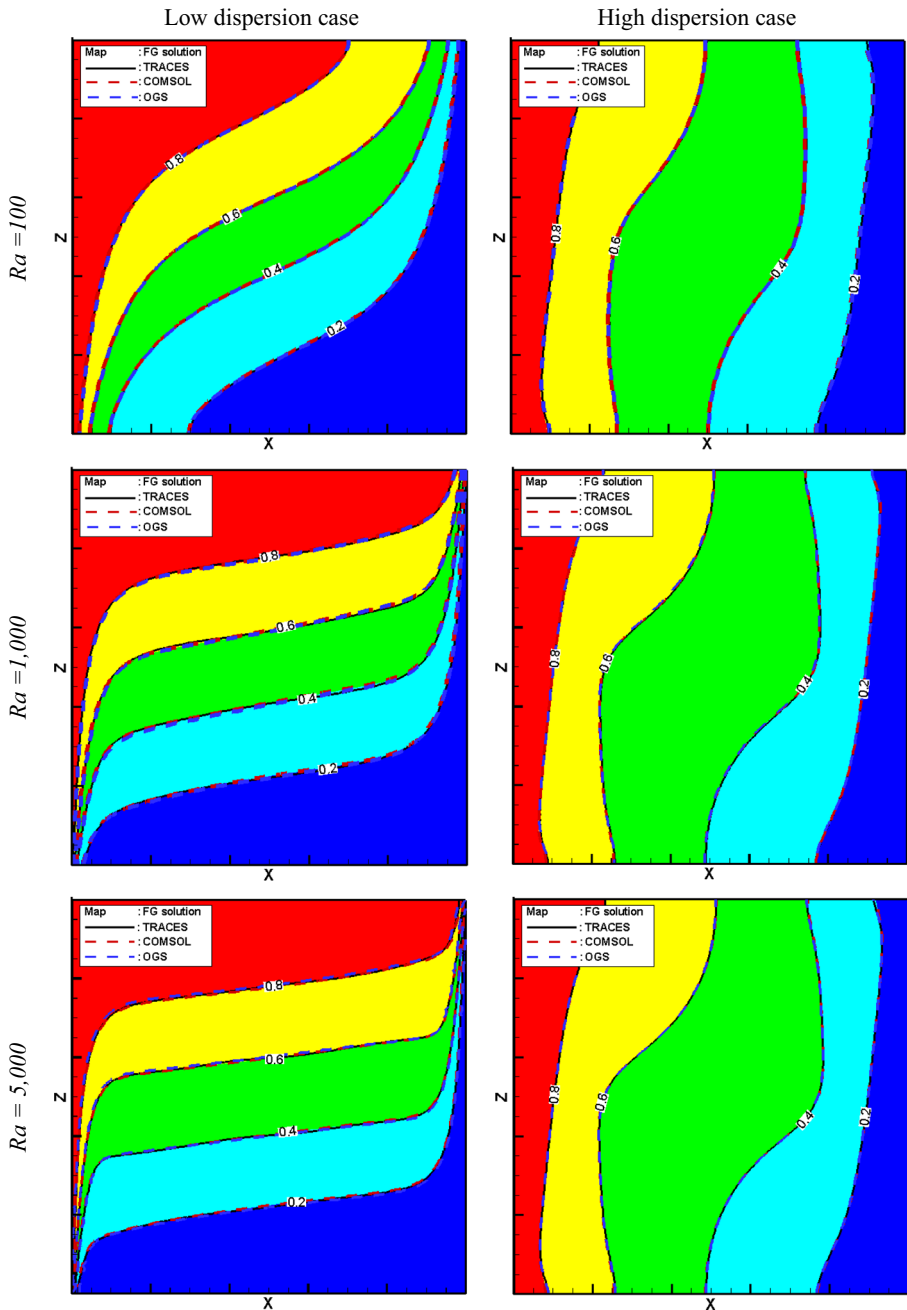


Fig. 7 Main isotherms (0.2, 0.4, 0.6 and 0.8): Comparison between the FG, TRACES, COMSOL and OGS solutions for the six test-case examples for $Ra = 100, 1000$ and 5000 in the case of low dispersion ($A_L = 0.001$) and high dispersion ($A_L = 1$) coefficients ($R_{\alpha_{\text{disp}}} = 0.1$ for all cases)

Table 1 The non-dimensional metrics obtained using the FG solution, TRACES (in-house code), OpenGeoSys (OGS) and COMSOL for the low dispersion case (referred to as “L-disp”) and the high dispersion case (referred to as “H-disp”). “Er” is the relative error calculated by assuming the FG values’ as error-free references

	Code	\overline{Nu}	$Er_{\overline{Nu}}$	θ^{top}	$Er_{\theta^{top}}$	U^{top}	$Er_{U^{top}}$	V^{top}	$Er_{V^{top}}$
Ra = 100									
L-Disp	FG	3.14	–	0.86	–	17.67	–	35.94	–
	TRACES	3.14	0.0%	0.86	0.0%	17.74	0.39%	35.20	2.05%
	OGS	3.11	0.95%	0.86	0.0%	17.90	1.30%	36.64	1.94%
	COMSOL	3.11	0.95%	0.86	0.0%	17.92	1.41%	36.55	1.69%
H-Disp	FG	7.98	–	0.59	–	24.40	–	37.11	–
	TRACES	8.01	0.37%	0.59	0.0%	24.32	0.32%	36.57	1.45%
	OGS	8.05	0.87%	0.59	0.0%	24.55	0.61%	37.61	1.91%
	COMSOL	8.01	0.37%	0.59	0.0%	24.61	0.86%	37.82	1.34%
Ra = 1000									
L-Disp	FG	15.51	–	0.94	–	83.26	–	408.39	–
	TRACES	15.72	1.35%	0.94	0.0%	83.43	0.20%	400.33	1.97%
	OGS	15.09	2.70%	0.94	0.0%	84.66	1.68%	417.38	2.20%
	COMSOL	15.12	2.51%	0.94	0.0%	84.69	1.71%	420.92	3.06%
H-Disp	FG	69.01	–	0.6	–	232.06	–	381.02	–
	TRACES	68.55	0.66%	0.6	0.0%	234.39	1.00%	380.45	0.14%
	OGS	69.14	0.36%	0.6	0.0%	234.04	0.85%	387.01	1.57%
	COMSOL	69.26	0.18%	0.6	0.0%	235.43	1.45%	387.43	1.68%
Ra = 5000									
L-Disp	FG	66.05	–	0.97	–	301.41	–	2173.90	–
	TRACES	62.72	5.04%	0.96	1.03%	297.84	1.18%	2107.88	3.03%
	OGS	58.11	12.00%	0.96	1.03%	305.12	1.23%	2254.12	3.69%
	COMSOL	57.18	13.42%	0.96	1.03%	304.90	1.15%	2236.25	2.86%
H-Disp	FG	341.95	–	0.61	–	1154.32	–	1910.64	–
	TRACES	337.04	1.43%	0.61	0.0%	1167.61	1.15%	1899.83	0.56%
	OGS	339.11	0.83%	0.61	0.0%	1159.91	1.28%	1914.04	0.17%
	COMSOL	343.04	0.31%	0.61	0.0%	1169.21	0.48%	1924.10	0.70%

is because TRACES is based on the DG method which allows numerical dispersion to be reduced (Younes and Ackerer 2008; Nguyen et al. 2009; Dijoux et al. 2019).

The comparisons developed in this section show the sensitivity of the solutions to the numerical method used for solving the governing equation. The results presented in Table 1 provide high-quality data that is useful for testing numerical codes dealing with NC in porous media. While Fig. 7 provides a qualitative comparison of the solutions, Table 1 allows for a quantitative comparison based on numerical indicators that are more rigorous for benchmarking than visual inspection (Prasad and Simmons 2005).

The buoyancy effects in COMSOL model are implemented by setting up the density as a function of temperature. Thus, the density is dependent on temperature in all terms of the governing equation. This means that the COMSOL model is based on the full nonlinear model without Boussinesq approximation which assumes temperature-dependent density only in the buoyancy term. The good agreement between the COMSOL results and the FG

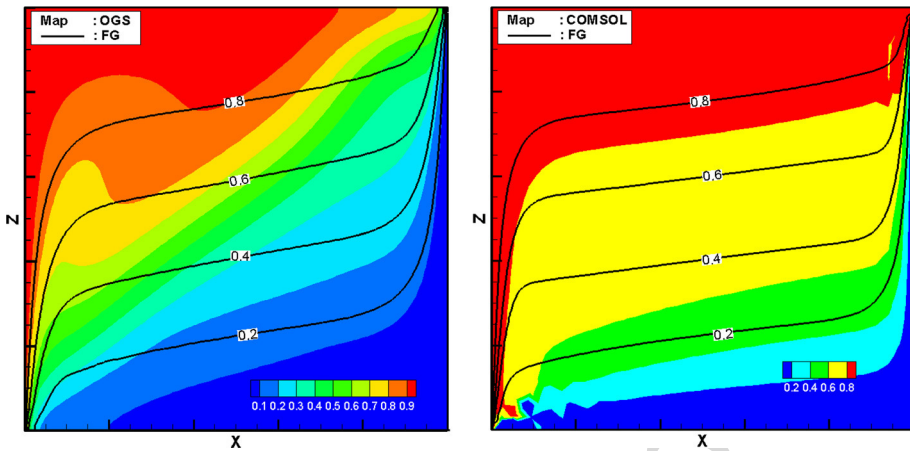


Fig. 8 Temperature distribution: examples of inconsistent results obtained with OGS (left, $Ra = 1000$) and COMSOL (right, $Ra = 5000$). For OGS (mesh of 10 K nodes), inconsistency is related to the adaptive time integration scheme. This error can be removed by imposing a relatively small maximum time step size. For COMSOL (mesh of 2 K nodes), the error appears as unphysical oscillations. These oscillations can be avoided by using a stabilization technique

667 solution provides preliminary insights into the validity of the Boussinesq approximation in
 668 the presence of thermal dispersion in NC in a porous enclosure.

669 **4.3 Effects of Longitudinal and Transverse Dispersion Coefficients: Correlation** 670 **of the Nusselt Number with the Dispersion Coefficients**

671 As it can be concluded from the scaled equations, the temperature distribution, heat flux and
 672 velocity field are controlled by three non-dimensional parameters: Ra (Rayleigh number),
 673 A_L (longitudinal dispersion coefficient) and $R_{\alpha_{disp}}$ (ratio of α_T to α_L). Here we use the
 674 developed FG solution to examine the role of the dispersion coefficients A_L and $R_{\alpha_{disp}}$ on
 675 the convective flow and heat transfer processes, for three values of Rayleigh number (100,
 676 1000 and 5000). For each value of Ra , we carried out 48 simulations by uniformly varying
 677 A_L between 0.01 and 1 and $R_{\alpha_{disp}}$ between 0.04 and 1 (8 values for A_L and 6 values for
 678 $R_{\alpha_{disp}}$). These ranges cover most typical field applications (Abarca et al. 2007). Thus, a total
 679 of 144 cases were performed. In all the runs, we used the highest numbers of FSMs (18,000)
 680 to be on the safe side when varying the parameters. As a quantity of interest, we consider
 681 the temperature (based on square grid 50×50 nodes), the Nusselt number and the maximum
 682 velocity components (U^{\max} and V^{\max}). The 144 simulations developed for the parameter
 683 sensitivity analysis have been done efficiently with reduced computational time due to the
 684 high computational performance of the FG solution.

685 Figure 9 depicts the variations of U^{\max} , V^{\max} and \overline{Nu} for the three Rayleigh number
 686 regimes. The first observation is that U^{\max} and V^{\max} both increase with Ra . Thus, as with
 687 the purely diffusive model, the increase in Rayleigh number intensifies the rotating convective
 688 flow no matter what the range of the dispersion coefficients. This is consistent with the analysis
 689 in the previous section based on streamlines. U^{\max} is almost insensitive to A_L , especially at
 690 high Rayleigh numbers. For the high and intermediate Rayleigh numbers, at constant $R_{\alpha_{disp}}$,
 691 the effect of A_L on U^{\max} indicates two regimes. We have increasing variation when A_L is

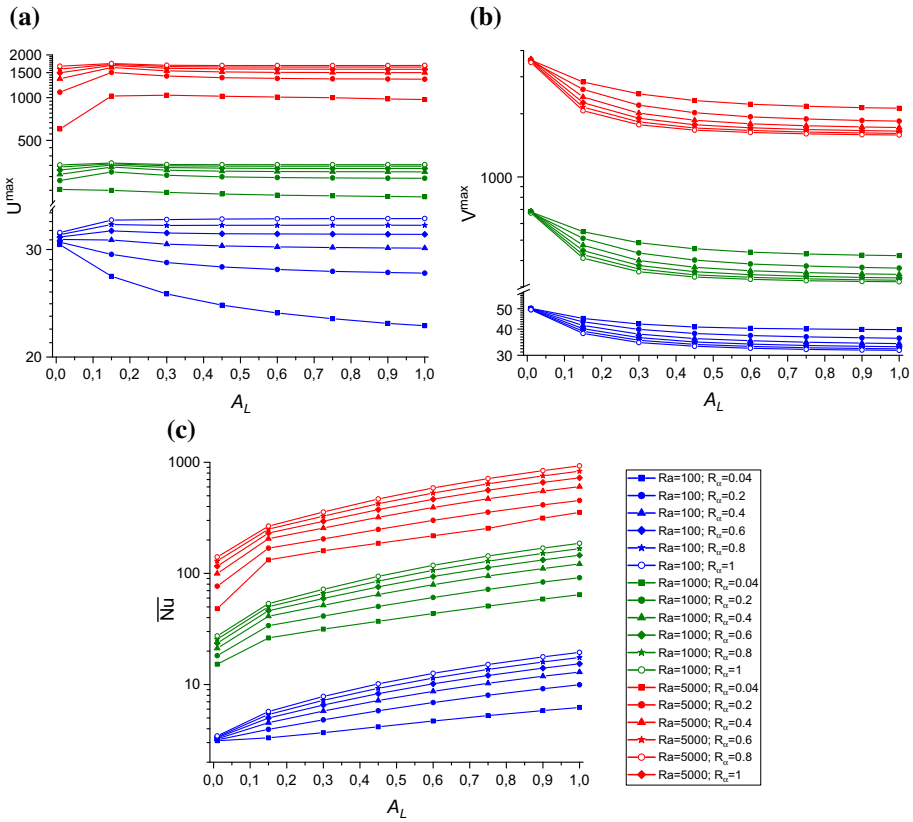


Fig. 9 Variations of U^{\max} , V^{\max} and \overline{Nu} with A_L and $R_{\alpha_{\text{disp}}}$ at low (blue), intermediate (green) and high (red) Rayleigh numbers

692 small (less than 0.15) and a slight decrease for higher A_L . This transition regime does not exist
 693 in the case of low Rayleigh number and small value of $R_{\alpha_{\text{disp}}}$ where U^{\max} is continuously
 694 decreasing. Figure 9a shows that at constant A_L , U^{\max} increases with $R_{\alpha_{\text{disp}}}$. Important
 695 variations can be observed for the lowest values of $R_{\alpha_{\text{disp}}}$. For the highest values, U^{\max}
 696 becomes slightly sensitivity to $R_{\alpha_{\text{disp}}}$. V^{\max} decreases with A_L (Fig. 9b). This confirms that
 697 the increase in A_L enhances the mixing between hot and cold fluids. Such mixing dissipates
 698 the buoyancy forces and dampens the fluid circulation. From Fig. 9b, it can be observed that
 699 $R_{\alpha_{\text{disp}}}$ has a slight effect and in contrast to U^{\max} , V^{\max} decreases with $R_{\alpha_{\text{disp}}}$. Thus, $R_{\alpha_{\text{disp}}}$
 700 has contradictory effects on U^{\max} and V^{\max} .

701 Figure 9c shows that, as for the purely thermal diffusive model, the average Nusselt
 702 number increases with Ra . This is mainly related to the intensification of the rotating flow
 703 associated with the increase of Ra . From Fig. 9c, it can be observed that, at constant A_L ,
 704 the Nusselt number increases with $R_{\alpha_{\text{disp}}}$. This makes sense regarding the expression of \overline{Nu} .
 705 (Eq. 32). Despite the fact that the vertical velocity component along the hot wall decreases
 706 with increasing A_L , this is associated with a decrease of \overline{Nu} . The increase of A_L pushes
 707 the 0.9 and 0.1 isotherms toward the vertical wall and as a result increases the temperature
 708 gradient which is directly related to the average Nusselt number.

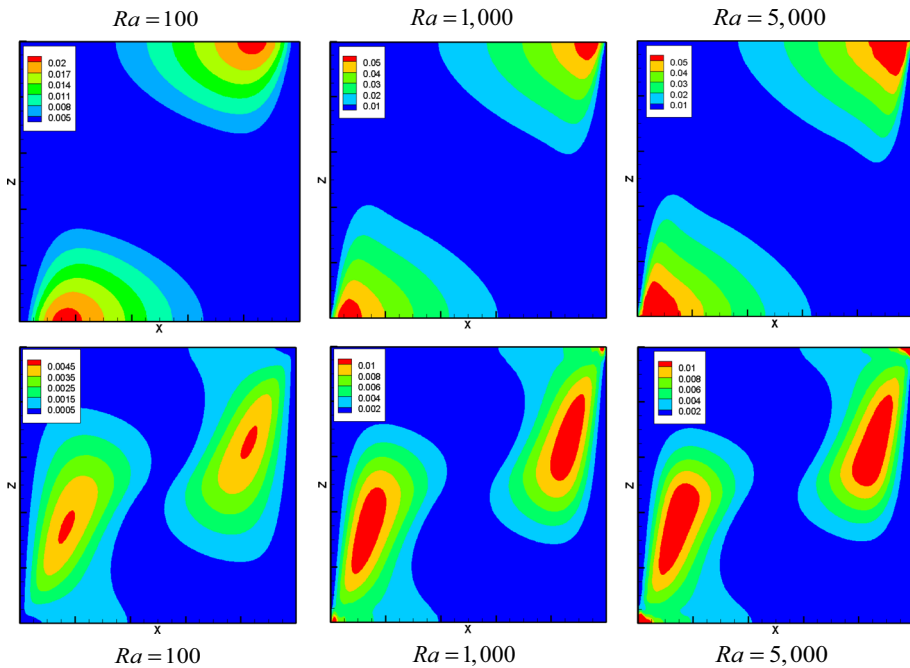


Fig. 10 Spatial map of the temperature variance. At top variable A_L is variable between 0.01 and 1 and $R_{\alpha_{\text{disp}}}$ is constant ($= 0.4$) and at bottom variable $R_{\alpha_{\text{disp}}}$ (0.04 – 1) and constant $A_L (= 0.3)$

709 The effects of A_L and R_{α} on the temperature distribution are investigated in Figs. 10
 710 and 11, respectively. Figure 10 (top) shows the temperature variance of a sample of eight
 711 simulations performed by varying A_L between 0.01 and 1 while keeping $R_{\alpha_{\text{disp}}}$ constant
 712 ($= 0.4$). The variance maps show that the temperature distribution is mostly sensitive to A_L
 713 along the adiabatic top and bottom surface, toward the bottom-left and top-right corners,
 714 respectively. This is consistent with the results obtained in Fig. 6a which shows that the
 715 longitudinal dispersive flux is important in these zones as the velocity is parallel to the
 716 temperature gradient. A slight difference can be observed between the variance maps at Ra
 717 $= 1000$ and 5000 . This means that at high Rayleigh numbers the temperature distribution
 718 is mainly controlled by the dispersion coefficient. The behavior of the main isotherms as
 719 A_L varies is depicted in Fig. 11a. This figure shows the main isotherms (0.1, 0.5 and 0.9)
 720 at $Ra = 100$, $R_{\alpha_{\text{disp}}} = 0.4$ and for eight different values of A_L ranging between 0.01 and
 721 1. For the sake of brevity, we only present the results for $Ra = 100$. Similar behaviors have
 722 been observed at $Ra = 1000$ and 5000 . Figure 11a shows that the 0.5 isotherm is more
 723 affected by A_L than other isotherms. The increase of A_L intensifies the mixing related to the
 724 thermal dispersion which widens the mixing zone. This pushes the hot isotherm (0.9) toward
 725 the hot wall at the top part of the cavity and leads to greater intrusion of isotherms in the
 726 lower part. Symmetrical behavior occurs for the cold isotherm (0.1). The 0.5 isotherm moves
 727 toward the hot wall (at the top) when A_L is increased, as this latter dampens the convective
 728 flow.

729 Figure 10 (bottom) shows that, whatever the Rayleigh number, the temperature distri-
 730 butions are less sensitive to $R_{\alpha_{\text{disp}}}$ than A_L (see scale levels on that figure). The zones of

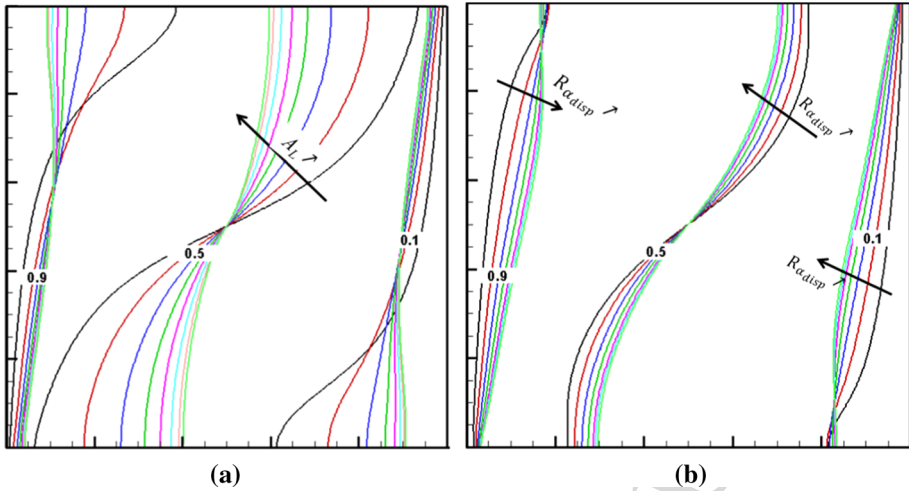


Fig. 11 Variations of the main isotherms (0.1, 0.5 and 0.9) for $Ra = 100$: a) with respect to A_L at constant $R_{\alpha_{disp}} (= 0.4)$ and b) with respect to $R_{\alpha_{disp}}$ at constant $A_L (= 0.3)$. The arrows indicate increasing variation of A_L and $R_{\alpha_{disp}}$

influence of $R_{\alpha_{disp}}$ expand vertically in front of the vertical walls toward the bottom and top corners at the hot and cold walls, respectively. This is consistent with the discussion about the transverse heat flux in Fig. 6b. The variation of the main isotherms with respect to $R_{\alpha_{disp}}$ (at constant A_L) is depicted in Fig. 10b. For the 0.5 isotherm, similar to the variation with respect to A_L , this isotherm moves left (resp. right) at the top (resp. bottom) part of the domain. The increase of $R_{\alpha_{disp}}$ leads to greater intrusion of the hot (0.9) and cold (0.1) isotherms.

The correlation of the average Nusselt number to the Rayleigh number in many configurations of internal NC has been widely investigated in the literature. However, to the best of our knowledge, no correlation study has been done in the presence of thermal dispersion. Thus, here we present a preliminary correlation study based on the developed FG solution. In the presence of dispersion, the average Nusselt number is function of Ra , A_L and $R_{\alpha_{disp}}$. We used the MATLAB curve fitting tool (CFTool) with the results of the 144 runs (presented above) to find this correlation. However, it was quite difficult to find a single correlation for three values of Rayleigh number. Thus, we develop a correlation for each value. The best fittings have been obtained using surface polynomial correlations:

$$\overline{Nu} = \sum_{i=1}^{n_A} \sum_{j=1}^{n_R} P_{i,j} A_L^i R_{\alpha}^j \tag{37}$$

For $Ra = 100$, the results reveal strong correlation (coefficient of determination $R^2 = 1$) with a polynomial of third degree ($n_A + n_R = 3$) (Fig. 12a). When Rayleigh number is increased, the variation of \overline{Nu} becomes more complex. Higher polynomial degrees should be used in these cases. For $Ra = 1000$ and 5000 , good regressions have been obtained using polynomials of degree 4 and 5, respectively (Fig. 12b, c). The polynomial coefficients for the three correlations are summarized in “Appendix C.”

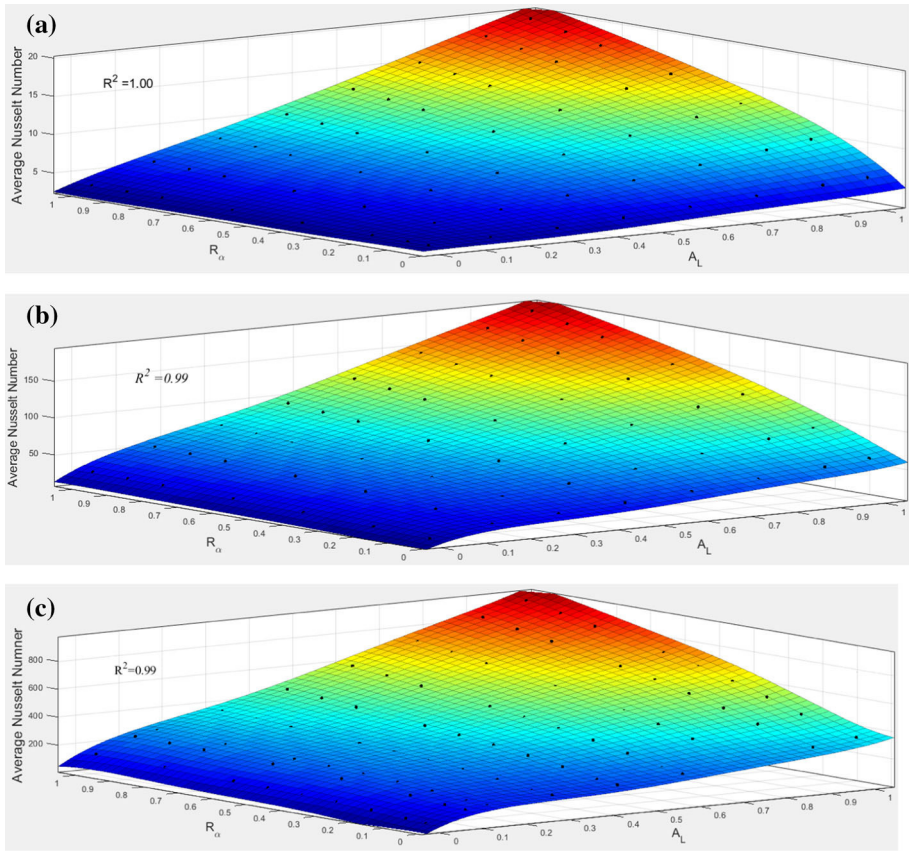


Fig. 12 Variation of the average Nusselt number with respect to A_L and $R_{\alpha_{disp}}$ with the corresponding regression surface for **a** $Ra = 100$, **b** 1000 and **c** 5000

5 Conclusion

This study presents a comprehensive analysis of the effect of thermal dispersion on internal NC in a square porous enclosure. A vertically oriented porous square cavity with heated vertical walls is investigated. Thermal dispersion is modeled using a velocity-dependent anisotropic dispersion tensor, introducing longitudinal and transverse dispersion coefficients. A high-accuracy solution is developed using the FG method applied to the stream function formulation of the governing equation. A sound implementation is developed to obtain accurate solutions with optimized CPU time. In the spectral space, the velocity field is expressed analytically in terms of temperature, and the spectral system is solved with the Fourier coefficients of the temperature as the primary unknown. Comparisons against TRACES (in-house code), OGS and COMSOL highlight the worthiness of the developed FG solution as a benchmark to validate and compare numerical codes. For low Rayleigh numbers, the FG solutions are in excellent agreement with TRACES, COMSOL and OGS. For high Rayleigh numbers, the FG solution shows high accuracy as it avoids numerical artifacts related to spatial and time discretization, encountered with standard methods. High-quality data based on quantitative indicators, suitable for code benchmarking, are provided. The FG solution is used to obtain

771 a more comprehensive understanding of thermal dispersion processes on NC. In the pres-
 772 ence of thermal dispersion, the isotherms are different from those observed with the purely
 773 diffusive model. Their zigzag shape is mainly related to the velocity-dispersion processes.
 774 The longitudinal dispersive flux is important toward the adiabatic walls where the velocity
 775 is parallel to the temperature gradient. Conversely, the longitudinal flux is important in front
 776 of the isothermal walls where the velocity is perpendicular to the temperature gradient.

777 A total of 144 runs of the FG method have been performed by varying the dispersion
 778 coefficients for three Rayleigh regimes (100, 1000 and 5000) in order to understand the
 779 effects of these dispersion parameters on fluid flow and heat transfer. In general, increasing
 780 A_L (non-dimensional longitudinal dispersion coefficient) and $R_{\alpha_{disp}}$ (the ratio of transverse
 781 to longitudinal dispersion coefficients) dampens the fluid circulation and increases the heat
 782 transfer to the domain. A_L and $R_{\alpha_{disp}}$ control the temperature distribution at high Rayleigh
 783 numbers. The isotherms are mainly affected by A_L near the adiabatic walls. $R_{\alpha_{disp}}$ affects the
 784 isotherms near the isothermal walls. The FG solutions were used to explore the correlation
 785 between the Nusselt number and the dispersion coefficients (A_L and $R_{\alpha_{disp}}$). Polynomial
 786 correlations have been derived for three Rayleigh regimes.

787 Despite the importance of the problem of NC in porous square enclosure, previous works
 788 assumed pure thermal diffusion. The subject of this paper was to examine the effect of thermal
 789 dispersion on the heat flux and convective flow structure and to provide a new understanding
 790 of the thermal dispersion processes. Due to the simplicity of the boundary conditions, the
 791 porous square enclosure is commonly accepted as benchmark for testing numerical codes and
 792 schemes. Accurate solutions of this problem, suitable for benchmarking, have been the subject
 793 of several previous works. All of the previously developed solutions are limited to purely
 794 thermal diffusion. Here, we develop, for the first time, accurate solutions for cases including
 795 thermal dispersion and we highlight the worthiness of these cases as benchmarks. We provide
 796 a new unambiguous benchmark that is more representative of physical processes than the
 797 purely diffusive one. From a numerical point of view, this work represents a generalization of
 798 the FG method to deal with natural convection in porous enclosures in the case of velocity-
 799 dependent dispersion tensor. Furthermore, an important technical feature of this work is that
 800 the problem of natural convection in a square porous cavity can be solved in the spectral
 801 space using only temperature as primary unknown. We expect that this approach can be
 802 applied to other porous cavity geometries. The developed FG solution is limited to steady
 803 state. Extension of this work to transient cases is worthy of future inquiry.

804 The source code of the Fourier series solution and TRACES with several test examples are
 805 available on the author’s Web site (<https://lhyges.unistra.fr/FAHS-Marwan>). The developed
 806 COMSOL and OGS models are uploaded on the software exchange Web sites.

807 **Appendix A: Coefficients of the Spectral System**

808 The coefficients of Eqs. (27) and (28) are defined as follows:

$$809 \quad A_{i,j} = \begin{cases} 0 & \text{if } i = j \\ \frac{1-(-1)^{i+j}}{i+j} + \frac{1-(-1)^{i-j}}{i-j} & \text{if } i \neq j \end{cases} \quad (A.1)$$

$$812 \quad e^g = \begin{cases} 2 & g = 0 \\ 1 & g \neq 0 \end{cases} \quad (A.2)$$

$$813 \quad \tilde{B}_{g,h} = \begin{cases} B_{g,h} & \text{if } g \leq Nm \text{ and } h \leq Nn \\ 0 & \end{cases} \quad (A.3)$$

$$\begin{aligned}
 \beta_{g,m,r}^I &= \delta_{g,r-m} + \delta_{g,m-r} + \delta_{g,m+r} \\
 \beta_{g,m,r}^{II} &= \delta_{g,r-m} - \delta_{g,r+m} + \delta_{g,m-r} \\
 \chi_{h,n,s}^I &= \delta_{h,s+n} - \delta_{h,s-n} + \delta_{h,n-s} \\
 \chi_{h,n,s}^{II} &= \delta_{h,n+s} - \delta_{h,n-s} + \delta_{h,s-n}
 \end{aligned} \tag{A.4}$$

820 Appendix B: Physical Parameters Used in TRACES, COMSOL and OGS

See Table 2.

Table 2 Dimensional parameters for the six test cases

Physical parameters	Value
Square size (m)	$H = 1$
Cold water density (kg m^{-3})	$\rho_c = 1000$
Coefficient of thermal expansion ($^{\circ}\text{C}^{-1}$)	$\beta = 0.01$
Hot wall temperature ($^{\circ}\text{C}$)	$T_h = 1$
Cold wall temperature ($^{\circ}\text{C}$)	$T_c = 0$
Porosity (-)	0.1
Permeability (m^2)	$K = 3.36 \times 10^{-10}$ (for Ra = 100) $K = 3.36 \times 10^{-9}$ (for Ra = 1000) $K = 16.8 \times 10^{-9}$ (for Ra = 5000)
Gravity acceleration (m s^{-2})	$g = 9.8$
Viscosity ($\text{kg m}^{-1} \text{s}^{-1}$)	$\mu = 10^{-3}$
Fluid thermal conductivity ($\text{w m}^{-1} \text{ }^{\circ}\text{C}^{-1}$)	0.65
Solid grains thermal conductivity ($\text{w m}^{-1} \text{ }^{\circ}\text{C}^{-1}$)	1.59
Fluid specific heat ($\text{J kg }^{\circ}\text{C}^{-1}$)	4200
Solid grains specific heat ($\text{J kg }^{\circ}\text{C}^{-1}$)	580
Solid grains density	2000
Longitudinal dispersion coefficient (m)	1, 0 (for the high dispersion case) 0.001 (for the low dispersion case)
Transverse dispersion coefficient (m)	0, 1 (for the high dispersion case) 0.0001 (for the low dispersion case)

821

822 Appendix C: Coefficients for the Polynomial Correlations 823 of the Average Nusselt Number

See Table 3.

Table 3 Coefficients of the polynomials used for the correlation between the average Nusselt number and the dispersion coefficients (A_L and $R_{\alpha\text{disp}}$)

Coef	Ra = 100	Ra = 1000	Ra = 5000	Coef	Ra = 100	Ra = 1000	Ra = 5000
$P_{0,0}$	2.82	12.84	38.76	$P_{3,0}$	-0.0284	423.6	1.03×10^4
$P_{0,1}$	3.447	22.66	-50.6	$P_{3,1}$	0.00	-14.02	-584.7
$P_{0,2}$	-7.59	-7.071	1634	$P_{3,2}$	0.00	0.00	250.6
$P_{0,3}$	4.83	-12.18	-4755				
$P_{0,4}$	0.00	9.46	5392				
$P_{0,5}$	0.00	0.00					
$P_{1,0}$	1.283	116.3	1172	$P_{4,0}$	0.00	-185	-9581
$P_{1,1}$	19.94	147.8	112.3	$P_{4,1}$	0.00	0.00	9.327
$P_{1,2}$	-7.052	-77.11	989.6				
$P_{1,3}$	0.00	22.3	-1867				
$P_{1,4}$	0.00	0.00	1022				
$P_{2,0}$	1.433	-311.6	-4957	$P_{5,0}$	0.00	0.00	3309
$P_{2,1}$	0.3226	35.34	736.6				
$P_{2,2}$	0.00	2.744	196.3				
$P_{2,3}$	0.00	0.00	-350.1				

824

References

- 826 Abarca, E., Carrera, J., Sánchez-Vila, X., Dentz, M.: Anisotropic dispersive Henry problem. *Adv. Water*
827 *Resour.* **30**, 913–926 (2007). <https://doi.org/10.1016/j.advwatres.2006.08.005>
- 828 Abbas, I.A., El-Amin, M.F., Salama, A.: Effect of thermal dispersion on free convection in a fluid saturated
829 porous medium. *Int. J. Heat Fluid Flow* **30**, 229–236 (2009). <https://doi.org/10.1016/j.ijheatfluidflow.2009.01.004>
- 830 Ameli, A.A., Craig, J.R.: Semi-analytical 3D solution for assessing radial collector well pumping impacts on
831 groundwater–surface water interaction. *Hydrol. Res.* **49**, 17–26 (2018). <https://doi.org/10.2166/nh.2017.201>
- 832 Ameli, A.A., Craig, J.R., Wong, S.: Series solutions for saturated–unsaturated flow in multi-layer unconfined
833 aquifers. *Adv. Water Resour.* **60**, 24–33 (2013). <https://doi.org/10.1016/j.advwatres.2013.07.004>
- 834 Asbik, M., Zeghmati, B., Louahlia-Gualous, H., Yan, W.M.: The effect of thermal dispersion on free convection
835 film condensation on a vertical plate with a thin porous layer. *Transp. Porous Media* **67**, 335–352 (2007).
836 <https://doi.org/10.1007/s11242-006-9028-9>
- 837 Ataie-Ashtiani, B., Simmons, C.T., Irvine, D.J.: Confusion about “convection”! *Groundwater* **56**, 683–687
838 (2018). <https://doi.org/10.1111/gwat.12790>
- 839 Bear, J., Bachmat, Y.: *Introduction to Modeling of Transport Phenomena in Porous Media*. Springer, Dordrecht
840 (1990)
- 841 Bañri, A., Zarco-Pernia, E., García de María, J.-M.: A review on natural convection in enclosures for engineering
842 applications. The particular case of the parallelogrammic diode cavity. *Appl. Therm. Eng.* **63**, 304–322
843 (2014). <https://doi.org/10.1016/j.applthermaleng.2013.10.065>
- 844 BniLam, N., Al-Khoury, R.: A spectral element model for nonhomogeneous heat flow in shallow geothermal
845 systems. *Int. J. Heat Mass Transf.* **104**, 703–717 (2017). <https://doi.org/10.1016/j.ijheatmasstransfer.2016.08.055>
- 846 Cheng, P.: Thermal dispersion effects in non-Darcian convective flows in a saturated porous medium. *Lett.*
847 *Heat Mass Transf.* **8**, 267–270 (1981). [https://doi.org/10.1016/0094-4548\(81\)90041-2](https://doi.org/10.1016/0094-4548(81)90041-2)
- 848
- 849
- 850


- 851 Cheng, W.T., Lin, H.T.: Unsteady forced convection heat transfer on a flat plate embedded in the fluid-saturated
 852 porous medium with inertia effect and thermal dispersion. *Int. J. Heat Mass Transf.* **45**, 1563–1569 (2002).
 853 [https://doi.org/10.1016/S0017-9310\(01\)00235-6](https://doi.org/10.1016/S0017-9310(01)00235-6)
- 854 DeGroot, C.T., Straatman, A.G.: Thermal Dispersion in High-Conductivity Porous Media. In: Delgado,
 855 J.M.P.Q., de Lima, A.G.B., da Silva, M.V. (eds.) *Numerical Analysis of Heat and Mass Transfer in*
 856 *Porous Media*, pp. 153–180. Springer, Berlin (2012)
- 857 Diersch, H.-J.G.: *FEFLOW*. Springer, Berlin (2014)
- 858 El-Hakim, M.A.: Thermal dispersion effects on combined convection in non-Newtonian fluids along a non-
 859 isothermal vertical plate in a porous medium. *Transp. Porous Media* **45**, 29–40 (2001). [https://doi.org/](https://doi.org/10.1023/A:1011867113620)
 860 [10.1023/A:1011867113620](https://doi.org/10.1023/A:1011867113620)
- 861 Dijoux, L., Fontaine, V., Mara, T.A.: A projective hybridizable discontinuous Galerkin mixed method for
 862 second-order diffusion problems. *Appl. Math. Model.* **75**, 663–677 (2019). [https://doi.org/10.1016/j.](https://doi.org/10.1016/j.apm.2019.05.054)
 863 [apm.2019.05.054](https://doi.org/10.1016/j.apm.2019.05.054)
- 864 Emami-Meybodi, H.: Dispersion-driven instability of mixed convective flow in porous media. *Phys. Fluids*
 865 **29**, 094102 (2017). <https://doi.org/10.1063/1.4990386>
- 866 Fahs, M., Younes, A., Mara, T.A.: A new benchmark semi-analytical solution for density-driven flow in porous
 867 media. *Adv. Water Resour.* **70**, 24–35 (2014). <https://doi.org/10.1016/j.advwatres.2014.04.013>
- 868 Fahs, M., Younes, A., Makradi, A.: A reference benchmark solution for free convection in a square cavity filled
 869 with a heterogeneous porous medium. *Numer. Heat Transf. B Fundam.* **67**, 437–462 (2015). [https://doi.](https://doi.org/10.1080/10407790.2014.977183)
 870 [org/10.1080/10407790.2014.977183](https://doi.org/10.1080/10407790.2014.977183)
- 871 Fahs, M., Ataie-Ashtiani, B., Younes, A., Simmons, C.T., Ackerer, P.: The Henry problem: new semianalytical
 872 solution for velocity-dependent dispersion. *Water Resour. Res.* **52**, 7382–7407 (2016). [https://doi.org/](https://doi.org/10.1002/2016WR019288)
 873 [10.1002/2016WR019288](https://doi.org/10.1002/2016WR019288)
- 874 Fajraoui, N., Fahs, M., Younes, A., Sudret, B.: Analyzing natural convection in porous enclosure with poly-
 875 nomial chaos expansions: effect of thermal dispersion, anisotropic permeability and heterogeneity. *Int.*
 876 *J. Heat Mass Transf.* **115**, 205–224 (2017). <https://doi.org/10.1016/j.ijheatmasstransfer.2017.07.003>
- 877 Guevara Morel, C.R., van Reeuwijk, M., Graf, T.: Systematic investigation of non-Boussinesq effects in
 878 variable-density groundwater flow simulations. *J. Contam. Hydrol.* **183**, 82–98 (2015). [https://doi.org/](https://doi.org/10.1016/j.jconhyd.2015.10.004)
 879 [10.1016/j.jconhyd.2015.10.004](https://doi.org/10.1016/j.jconhyd.2015.10.004)
- 880 Hirthe, E.M., Graf, T.: Non-iterative adaptive time-stepping scheme with temporal truncation error control
 881 for simulating variable-density flow. *Adv. Water Resour.* **49**, 46–55 (2012). [https://doi.org/10.1016/j.](https://doi.org/10.1016/j.advwatres.2012.07.021)
 882 [advwatres.2012.07.021](https://doi.org/10.1016/j.advwatres.2012.07.021)
- 883 Hooman, K., Li, J., Dahari, M.: Thermal dispersion effects on forced convection in a porous-saturated pipe.
 884 *Thermal Sci. Eng. Prog.* **2**, 64–70 (2017). <https://doi.org/10.1016/j.tsep.2017.04.005>
- 885 Hoteit, H., Ackerer, P., Mosé, R., Erhel, J., Philippe, B.: New two-dimensional slope limiters for discontinuous
 886 Galerkin methods on arbitrary meshes. *Int. J. Numer. Meth. Eng.* **61**, 2566–2593 (2004). [https://doi.org/](https://doi.org/10.1002/nme.1172)
 887 [10.1002/nme.1172](https://doi.org/10.1002/nme.1172)
- 888 Howle, L.E., Georgiadis, J.G.: Natural convection in porous media with anisotropic dispersive thermal con-
 889 ductivity. *Int. J. Heat Mass Transf.* **37**, 1081–1094 (1994). [https://doi.org/10.1016/0017-9310\(94\)90194-](https://doi.org/10.1016/0017-9310(94)90194-5)
 890 [5](https://doi.org/10.1016/0017-9310(94)90194-5)
- 891 Hsiao, S.: Natural convection in an inclined porous cavity with variable porosity and thermal dispersion effects.
 892 *Int. J. Numer. Meth. Heat Fluid Flow* **8**, 97–117 (1998). <https://doi.org/10.1108/09615539810198050>
- 893 Hsu, C.T., Cheng, P.: Thermal dispersion in a porous medium. *Int. J. Heat Mass Transf.* **33**, 1587–1597 (1990).
 894 [https://doi.org/10.1016/0017-9310\(90\)90015-M](https://doi.org/10.1016/0017-9310(90)90015-M)
- 895 Huddar, L.R.R.: Heat transfer in pebble-bed nuclear reactor cores cooled by fluoride salts. [https://cloudfront.](https://cloudfront.escholarship.org/dist/prd/content/qt3c69q4kf/qt3c69q4kf.pdf?t=otcme7)
 896 [escholarship.org/dist/prd/content/qt3c69q4kf/qt3c69q4kf.pdf?t=otcme7](https://cloudfront.escholarship.org/dist/prd/content/qt3c69q4kf/qt3c69q4kf.pdf?t=otcme7) (2016)
- 897 Imran, M.: An Experimental Study of Thermal and Thermohaline Convection in Saturated Porous Media
 898 (2013)
- 899 Ingham, D.B., Pop, I. (eds.): *Transport Phenomena in Porous Media*. Elsevier, Oxford (2005)
- 900 Jeong, N., Choi, D.H.: Estimation of the thermal dispersion in a porous medium of complex structures using
 901 a lattice Boltzmann method. *Int. J. Heat Mass Transf.* **54**, 4389–4399 (2011). [https://doi.org/10.1016/j.](https://doi.org/10.1016/j.ijheatmasstransfer.2011.05.003)
 902 [ijheatmasstransfer.2011.05.003](https://doi.org/10.1016/j.ijheatmasstransfer.2011.05.003)
- 903 Jha, B.K., Aina, B.: Numerical investigation of transient free convective flow in vertical channel filled with
 904 porous material in the presence of thermal dispersion. *Comput. Math. Model.* **28**, 350–367 (2017). [https://](https://doi.org/10.1007/s10598-017-9369-y)
 905 doi.org/10.1007/s10598-017-9369-y
- 906 Khaled, A.A., Chamkha, A.J.: Variable porosity and thermal dispersion effects on coupled heat and mass
 907 transfer by natural convection from a surface embedded in a non-metallic porous medium. *Int. J. Numer.*
 908 *Meth. Heat Fluid Flow* **11**, 413–429 (2001). <https://doi.org/10.1108/EUM0000000005530>
- 909 Kolditz, O., Bauer, S., Bilke, L., Böttcher, N., Delfs, J.O., Fischer, T., Görke, U.J., Kalbacher, T., Kosakowski,
 910 G., McDermott, C.I., Park, C.H., Radu, F., Rink, K., Shao, H., Shao, H.B., Sun, F., Sun, Y.Y., Singh,

- 911 A.K., Taron, J., Walther, M., Wang, W., Watanabe, N., Wu, Y., Xie, M., Xu, W., Zehner, B.: OpenGeoSys: an open-source initiative for numerical simulation of thermo-hydro-mechanical/chemical (THM/C) processes in porous media. *Environ. Earth Sci.* **67**, 589–599 (2012). <https://doi.org/10.1007/s12665-012-1546-x>
- 912
- 913
- 914
- 915 Kopriva, D.A.: *Implementing Spectral Methods for Partial Differential Equations*. Springer, Dordrecht (2009)
- 916 Kuznetsov, A.V.: Investigation of the effect of transverse thermal dispersion on forced convection in porous media. *Acta Mech.* **145**, 35–43 (2000). <https://doi.org/10.1007/BF01453643>
- 917
- 918 Languri, E., Pillai, K.: A combined experimental/numerical approach to study the thermal dispersion in porous media flows. *Therm. Sci.* **18**, 463–474 (2014). <https://doi.org/10.2298/TSCI110626009L>
- 919
- 920 Mahmud, S., Pop, I.: Mixed convection in a square vented enclosure filled with a porous medium. *Int. J. Heat Mass Transf.* **49**, 2190–2206 (2006). <https://doi.org/10.1016/j.ijheatmasstransfer.2005.11.022>
- 921
- 922 Malomar, G.E.B., Mbow, C., Tall, P.D., Gueye, A., Traore, V.B., Beye, A.C.: Numerical study of 2-D natural convection in a square porous cavity: effect of three mode heating. *Open J. Fluid Dyn.* **07**, 89–104 (2017). <https://doi.org/10.4236/ojfd.2017.71007>
- 923
- 924
- 925 Miller, C.T., Dawson, C.N., Farthing, M.W., Hou, T.Y., Huang, J., Kees, C.E., Kelley, C.T., Langtangen, H.P.: Numerical simulation of water resources problems: models, methods, and trends. *Adv. Water Resour.* **51**, 405–437 (2013). <https://doi.org/10.1016/j.advwatres.2012.05.008>
- 926
- 927 Mohammadien, A.A., El-Amin, M.F.: Thermal dispersion-radiation effects on non-darcy natural convection in a fluid saturated porous medium. *Transp. Porous Media* **40**, 153–163 (2000). <https://doi.org/10.1023/A:1006654309980>
- 928
- 929
- 930 Molina-Giraldo, N., Bayer, P., Blum, P.: Evaluating the influence of thermal dispersion on temperature plumes from geothermal systems using analytical solutions. *Int. J. Therm. Sci.* **50**, 1223–1231 (2011). <https://doi.org/10.1016/j.ijthermalsci.2011.02.004>
- 931
- 932
- 933 Mousavi, S.E., Pask, J.E., Sukumar, N.: Efficient adaptive integration of functions with sharp gradients and cusps in n-dimensional parallelepipeds. *Int. J. Numer. Meth. Eng.* **91**, 343–357 (2012). <https://doi.org/10.1002/nme.4267>
- 934
- 935
- 936 Nield, D.A., Bejan, A.: *Convection in Porous Media*. Springer, Cham (2017)
- 937
- 938 Nield, D.A., Simmons, C.T.: A brief introduction to convection in Porous Media. *Transp. Porous Media* (2018). <https://doi.org/10.1007/s11242-018-1163-6>
- 939
- 940 Nguyen, N.C., Peraire, J., Cockburn, B.: An implicit high-order hybridizable discontinuous Galerkin method for linear convection–diffusion equations. *J. Comput. Phys.* **228**, 3232–3254 (2009). <https://doi.org/10.1016/j.jcp.2009.01.030>
- 941
- 942
- 943 Özerinç, S., Yazıcıoğlu, A.G., Kakaç, S.: Numerical analysis of laminar forced convection with temperature-dependent thermal conductivity of nanofluids and thermal dispersion. *Int. J. Therm. Sci.* **62**, 138–148 (2012). <https://doi.org/10.1016/j.ijthermalsci.2011.10.007>
- 944
- 945
- 946 Ozgumus, T., Mobedi, M.: Effect of pore to throat size ratio on thermal dispersion in porous media. *Int. J. Therm. Sci.* **104**, 135–145 (2016). <https://doi.org/10.1016/j.ijthermalsci.2016.01.003>
- 947
- 948 Pedras, M.H.J., de Lemos, M.J.S.: Thermal dispersion in porous media as a function of the solid–fluid conductivity ratio. *Int. J. Heat Mass Transf.* **51**, 5359–5367 (2008). <https://doi.org/10.1016/j.ijheatmasstransfer.2008.04.030>
- 949
- 950
- 951 Peyret, R.: *Spectral Methods for Incompressible Viscous Flow*. Springer, Berlin (2013)
- 952
- 953 Piga, B., Casasso, A., Pace, F., Godio, A., Sethi, R.: Thermal impact assessment of groundwater heat pumps (GWHPs): rigorous vs simplified models. *Energies* **10**, 1385 (2017). <https://doi.org/10.3390/en10091385>
- 954
- 955 Plumb, A.: The effect of thermal dispersion on heat transfer in packed bed boundary layers. Presented at the proceeding ASME JSME thermal engineering joint conference 2, Tokyo, Japan (1983)
- 956
- 957 Prasad, A., Simmons, C.T.: Using quantitative indicators to evaluate results from variable-density groundwater flow models. *Hydrogeol. J.* **13**, 905–914 (2005). <https://doi.org/10.1007/s10040-004-0338-0>
- 958
- 959 Rossa, G.B., Cliffe, K.A., Power, H.: Effects of hydrodynamic dispersion on the stability of buoyancy-driven porous media convection in the presence of first order chemical reaction. *J. Eng. Math.* **103**, 55–76 (2017). <https://doi.org/10.1007/s10665-016-9860-z>
- 960
- 961 Sachse, A., Rink, K., He, W., Kolditz, O.: *OpenGeoSys-Tutorial*. Springer, Cham (2015)
- 962
- 963 Scheidegger, A.E.: General theory of dispersion in porous media. *J. Geophys. Res.* **66**, 3273–3278 (1961). <https://doi.org/10.1029/JZ066i010p03273>
- 964
- 965 Shao, Q., Fahs, M., Younes, A., Makradi, A.: A high-accurate solution for Darcy-Brinkman double-diffusive convection in saturated porous media. *Numer. Heat Transf. B Fundam.* **69**, 26–47 (2015). <https://doi.org/10.1080/10407790.2015.1081044>
- 966
- 967 Shao, Q., Fahs, M., Younes, A., Makradi, A., Mara, T.: A new benchmark reference solution for double-diffusive convection in a heterogeneous porous medium. *Numer. Heat Transf. B Fundam.* **70**, 373–392 (2016). <https://doi.org/10.1080/10407790.2016.1215718>
- 968
- 969

- 970 Shao, Q., Fahs, M., Hoteit, H., Carrera, J., Ackerer, P., Younes, A.: A 3-D semianalytical solution for density-
 971 driven flow in porous media. *Water Resour. Res.* **54**, 10094–10116 (2018). [https://doi.org/10.1029/](https://doi.org/10.1029/2018WR023583)
 972 [2018WR023583](https://doi.org/10.1029/2018WR023583)
- 973 Sheremet, M.A., Pop, I., Bachok, N.: Effect of thermal dispersion on transient natural convection in a wavy-
 974 walled porous cavity filled with a nanofluid: Tiwari and Das' nanofluid model. *Int. J. Heat Mass Transf.*
 975 **92**, 1053–1060 (2016). <https://doi.org/10.1016/j.ijheatmasstransfer.2015.09.071>
- 976 Sheremet, M.A., Revnic, C., Pop, I.: Free convection in a porous wavy cavity filled with a nanofluid using
 977 Buongiorno's mathematical model with thermal dispersion effect. *Appl. Math. Comput.* **299**, 1–15 (2017).
 978 <https://doi.org/10.1016/j.amc.2016.11.032>
- 979 Tan, H., Cheng, X., Guo, H.: Closed solutions for transient heat transport in geological media: new develop-
 980 ment, comparisons, and validations. *Transp. Porous Media* **93**, 737–752 (2012). [https://doi.org/10.1007/](https://doi.org/10.1007/s11242-012-9980-5)
 981 [s11242-012-9980-5](https://doi.org/10.1007/s11242-012-9980-5)
- 982 Telles, R.S., Trevisan, O.V.: Dispersion in heat and mass transfer natural convection along vertical bound-
 983 aries in porous media. *Int. J. Heat Mass Transf.* **36**, 1357–1365 (1993). [https://doi.org/10.1016/S0017-](https://doi.org/10.1016/S0017-9310(05)80103-6)
 984 [9310\(05\)80103-6](https://doi.org/10.1016/S0017-9310(05)80103-6)
- 985 Thiele, M.: Heat dispersion in stationary mixed convection flow about horizontal surfaces in porous media.
 986 *Heat Mass Transf.* **33**, 7–16 (1997). <https://doi.org/10.1007/s002310050156>
- 987 Vadász, P. (ed.): *Emerging Topics in Heat and Mass Transfer in Porous Media*. Springer, Dordrecht (2008)
- 988 Vafai, K. (ed.): *Porous media: Applications in Biological Systems and Biotechnology*. CRC Press, Boca Raton,
 989 FL (2011)
- 990 Vafai, K. (ed.): *Handbook of Porous Media*. CRC Press, Taylor & Francis Group, Boca Raton (2015)
- 991 Wang, L., Nakanishi, Y., Hyodo, A., Suekane, T.: Three-dimensional structure of natural convection in a porous
 992 medium: effect of dispersion on finger structure. *Int. J. Greenhouse Gas Control* **53**, 274–283 (2016).
 993 <https://doi.org/10.1016/j.ijggc.2016.08.018>
- 994 Wang, Y., Qin, G., He, W., Bao, Z.: Chebyshev spectral element method for natural convection in a porous
 995 cavity under local thermal non-equilibrium model. *Int. J. Heat Mass Transf.* **121**, 1055–1072 (2018).
 996 <https://doi.org/10.1016/j.ijheatmasstransfer.2018.01.024>
- 997 Wen, B., Chang, K.W., Hesse, M.A.: Rayleigh–Darcy convection with hydrodynamic dispersion. *Phys. Rev.*
 998 *Fluids* (2018). <https://doi.org/10.1103/PhysRevFluids.3.123801>
- 999 Yacine, L., Mojtabi, A., Bennacer, R., Khouzam, A.: Soret-driven convection and separation of binary mixtures
 1000 in a horizontal porous cavity submitted to cross heat fluxes. *Int. J. Therm. Sci.* **104**, 29–38 (2016). [https://](https://doi.org/10.1016/j.ijthermalsci.2015.12.013)
 1001 doi.org/10.1016/j.ijthermalsci.2015.12.013
- 1002 Younes, A., Ackerer, P.: Solving the advection-dispersion equation with discontinuous Galerkin and multipoint
 1003 flux approximation methods on unstructured meshes. *Int. J. Numer. Meth. Fluids* **58**, 687–708 (2008).
 1004 <https://doi.org/10.1002/flid.1783>
- 1005 Younes, A., Fahs, M., Ahmed, S.: Solving density driven flow problems with efficient spatial discretizations
 1006 and higher-order time integration methods. *Adv. Water Resour.* **32**, 340–352 (2009). [https://doi.org/10.](https://doi.org/10.1016/j.advwatres.2008.11.003)
 1007 [1016/j.advwatres.2008.11.003](https://doi.org/10.1016/j.advwatres.2008.11.003)
- 1008 Younes, A., Ackerer, P., Delay, F.: Mixed finite elements for solving 2-D diffusion-type equations. *Rev.*
 1009 *Geophys.* (2010). <https://doi.org/10.1029/2008RG000277>
- 1010 Zhu, Q.Y., Zhuang, Y.J., Yu, H.Z.: Entropy generation due to three-dimensional double-diffusive convection
 1011 of power-law fluids in heterogeneous porous media. *Int. J. Heat Mass Transf.* **106**, 61–82 (2017). [https://](https://doi.org/10.1016/j.ijheatmasstransfer.2016.10.050)
 1012 doi.org/10.1016/j.ijheatmasstransfer.2016.10.050

1013 **Publisher's Note** Springer Nature remains neutral with regard to jurisdictional claims in published maps and
 1014 institutional affiliations.

1015 Affiliations

1016 Marwan Fahs¹  · Thomas Graf² · Tuong Vi Tran² · Behzad Ataie-Ashtiani^{3,4} ·
 1017 Craig. T. Simmons⁴ · Anis Younes^{1,5,6}

1018 ✉ Marwan Fahs
 1019 fahs@unistra.fr

1020 ¹ Laboratoire d'Hydrologie et Geochemie de Strasbourg, University of Strasbourg/EOST/ENGEES,
 1021 CNRS, 1 Rue Blessig, 67084 Strasbourg, France

- 1022 2 Institute of Fluid Mechanics and Environmental Physics in Civil Engineering, Leibniz Universität
1023 Hannover, Appelstr. 9A, 30167 Hannover, Germany
- 1024 3 Department of Civil Engineering, Sharif University of Technology, PO Box 11155-9313, Tehran,
1025 Iran
- 1026 4 National Centre for Groundwater Research and Training, College of Science and Engineering,
1027 Flinders University, GPO Box 2100, Adelaide, SA 5001, Australia
- 1028 5 IRD UMR LISAH, 92761 Montpellier, France
- 1029 6 Laboratoire de Modélisation en Hydraulique et Environnement, Ecole Nationale d'Ingénieurs de
1030 Tunis, Tunis, Tunisia

Author Proof

uncorrected proof